

Abrupt ending of MJO by CCKW precipitation leaves swath of flooding across Indonesia

Natasha V. Senior^{1*} | Adrian J. Matthews² | Benjamin G. M. Webber¹ | Jaka A. I. Paski^{3,4} | Danang E. Nuryanto³ | Richard W. Jones⁵ | Donald S. Permana³ | Auliya'a H. Febriyanti⁶

¹Centre for Ocean and Atmospheric Sciences, School of Environmental Sciences and Climatic Research Unit, University of East Anglia, UK

²Centre for Ocean and Atmospheric Sciences, School of Environmental Sciences and School of Mathematics, University of East Anglia, UK

³Center for Research and Development, Indonesia Agency for Meteorology Climatology and Geophysics (BMKG), Jakarta, Indonesia

⁴Department of Geophysics, Graduate School of Science, Tohoku University, Sendai, Japan

⁵Met Office, Exeter, UK

⁶West Kalimantan Climatology Station, Indonesia Agency for Meteorology Climatology and Geophysics (BMKG), Mempawah, Indonesia

Correspondence

N. Senior, School of Environmental Sciences, University of East Anglia, Norwich, NR4 7TJ, UK.
Email: n.senior@uea.ac.uk

Funding information

Newton Fund, UK Met Office through the FORSEA project, Grant/Award Number: DN373682; UK Natural Environment

Research Council through the TerraMaris project, Grant/Award Number:

NE/R016704/1

Convectively coupled Kelvin waves (CCKWs) are eastward propagating weather systems that locally organise convection and are linked to precipitation extremes across the Maritime Continent (MC). They are often embedded in active Madden-Julian Oscillation (MJO) phases. The MJO also propagates eastwards but influences convection in the MC over longer timescales and larger areas. This paper examines a case study during July 2021 of multiple CCKWs and westward propagating inertio-gravity waves (WIGs) embedded within an active MJO. The final CCKW traversed the western MC causing precipitation extremes across equatorial Indonesia and East Malaysia that led to numerous reports of flooding and landslides, with western Borneo the worst affected region. The MJO event was abruptly terminated following the passage of this CCKW. Analysis of the total column water budget reveals that the precipitation rate exceeded the vertically integrated moisture flux convergence provided by the CCKW, drying out the atmosphere and suppressing further convection. The performance of the UK Met Office prediction model was evaluated for this case

study; parameterised convection configurations generally performed as well as or better than explicit convection models. This is possibly because they better represented the location and timing of the convective systems that developed because of interactions between the CCKWs and WIGs. This research highlights how CCKWs should not simply be viewed as convective systems that locally affect weather, but as having the potential to deliver larger-scale impacts over the entire equatorial Maritime Continent, when part of a complex multiscale interaction **with the diurnal cycle and the MJO, whereby** . Such interactions can involve the MJO **influences influencing** CCKWs downscale by providing enhanced convection **and CCKWs interact with the MJO upscale terminating convection** . Conversely, the suppressed phase of CCKWs can dampen the MJO convective signal and terminate MJO propagation. Whilst weather prediction models may accurately forecast rainfall associated with individual equatorial modes, capturing their combined effect remains a challenge.

KEYWORDS

convectively coupled equatorial wave, Kelvin wave, extreme precipitation, high impact weather, Borneo, tropical waves, Indonesia

1 | INTRODUCTION

1 Indonesia's many islands and shallow seas are archetypal of those of the Maritime Continent (MC) (Ramage, 1968), the
2 most convectively active region on Earth that fuels global circulation. Floods and landslides caused by precipitation
3 extremes are major hazards experienced by the country leading to loss of life and damage to infrastructure (Hai et al.,
4 2017; Latos et al., 2021; Hermawan et al., 2022; Purwaningsih et al., 2022; Lubis et al., 2022). Hence, understanding
5 key predictors of rainfall extremes is crucial for improving forecasts and disaster preparedness. Recent studies (Ferrett
6 et al., 2020; Lubis and Respati, 2021) have shown that equatorial waves are a key mode of daily rainfall variability.
7 These waves often closely resemble the dry theoretical solutions to the shallow water equations (Wheeler and Kiladis,
8 1999; Kiladis et al., 2009), modified by the effect of convection and the background state (Matthews, 2021) and
9 provide a source of predictability of high impact weather (Ferrett et al., 2023; Wolf et al., 2023).

10 The islands of Sumatra, Borneo and Sulawesi are located along the equator (Figure 1), where convectively coupled
11 Kelvin waves (CCKWs) are active due to their equatorially symmetric structures with maximum convergence and pre-
12 cipitation on the equator. Consequently, there is an increase in precipitation amplitudes and a factor of 2-4 increase
13 in the likelihood of observing extreme rainfall on days when the convergent phase of a CCKW is present (Ferrett et al.,

14 2020). Indeed, 90% of all floods in Sumatra have been linked to CCKWs (Baranowski et al., 2020). CCKWs travel
15 eastward along the equatorial waveguide and influence precipitation extremes in a particular region over the course
16 of 1–2 days. Baranowski et al. (2016) found that CCKWs with their convective phase arriving in time with that of
17 the diurnal cycle of precipitation at the west coast of Sumatra, had larger precipitation amplitudes than CCKWs that
18 arrived out of phase with the local diurnal cycle. The distance between the west coasts of Borneo and Sumatra is
19 approximately the same distance that a CCKW travels in one day (10° longitude). Baranowski et al. (2016) proposed
20 that CCKWs arriving in phase with the diurnal cycle at the west coast of Sumatra would then also arrive in phase
21 with the diurnal cycle of at the west coast of Borneo and through these “boosts” were more likely to traverse the MC.
22 Senior et al. (2023) found that CCKWs linked to precipitation extremes on the west coast of Sumatra modulate the
23 diurnal cycle by increasing its precipitation amplitude and displacing their combined convergence zone closer to the
24 coast causing an increase in rainfall that persists for around 36 hours, including during the night and the early morning.

25 Convection is also modulated on intraseasonal timescales by the Madden–Julian Oscillation (MJO) (Madden and
26 Julian, 1972). This manifests as an eastward propagating equatorial disturbance with phases of enhanced and sup-
27 pressed convection over the MC with a period of around 30–90 days. Precipitation extremes increase by a factor
28 of 2 in the presence of an active MJO (Da Silva and Matthews, 2021). CCKWs and the diurnal cycle itself are also
29 influenced by the MJO (Peatman et al., 2021) and exist in a complex multiscale environment also when involved in
30 precipitation extremes. For example, CCKWs were found to be the primary factor in all MJO-related flooding events
31 (Baranowski et al., 2020). Peatman et al. (2014) found that diurnal precipitation over the MC is enhanced ahead of
32 the arrival of the main convective envelope of the MJO (phases 2 and 3) and that 80% of the MJO precipitation
33 anomaly over the MC manifests as variability of the diurnal precipitation Peatman et al. (2014). These scale inter-
34 actions between different modes of equatorial rainfall variability have the potential for devastating impacts. On 22
35 January 2019 the city of Makassar in Sulawesi experienced its most severe flood on record; the main drivers of the
36 event were a CCKW and a convectively coupled equatorial Rossby wave (CCERW), both embedded within an active
37 MJO (Latos et al., 2021). Also in January 2020 there were record-breaking floods in Jakarta linked to the confluence
38 of several equatorial waves modes, the MJO as well as a cross equatorial northerly surge (Lubis et al., 2022).

39 ~~In general the diurnal cycle of rainfall over the MC is such that it tends to peak over the central islands and
40 mountainous regions in the local afternoon, approaching the coastal regions in the local evening and propagating
41 offshore overnight (Yang and Slingo, 2001; Yang and Slingo, 2008; Yang and Slingo, 2014). However there is significant
42 variability between different islands due to their shape, orientation and topography (Wei et al., 2020). The diurnal
43 cycle over the island of Borneo and surrounding seas involves peak nocturnal rainfall over the central mountains due to
44 the convergence of the sea breezes and simultaneously offshore propagation due to the evening land breeze. The west
45 coast of the island of Sumatra possess a unique diurnal cycle pattern comprised of slowly propagating density currents
46 ($3\text{--}5\text{ m s}^{-1}$) and fast propagating gravity waves that extend far offshore (16 m s^{-1}) (Bai et al., 2021; Bai et al., 2023).
47 Bai et al. (2021) found that this offshore propagation occurs most frequently during MJO phases 1–3 and is fastest
48 during boreal summer.~~

49 Often observed during active MJO phases are westward propagating inertio-gravity waves (WIGs) which are
50 strongly coupled to the diurnal cycle (Nakazawa, 1988; Takayabu, 1994; Kiladis et al., 2009). Ruppert and Zhang (2019)
51 found that these WIGs tend to be triggered during the convective phase of the local diurnal cycle and propagate at
52 speeds of around (17 m s^{-1}) arriving in time with the convective phases of local diurnal cycles across multiple islands.
53 This is similar to the diurnal phase-locking mechanism observed in Baranowski et al. (2016) through which CCKWs
54 are able to traverse the MC and it is possible that some WIGs may be generated by CCKWs themselves (Liebmann
55 et al., 1997). Furthermore, WIGs may also be important for local diurnal processes. The west coast of the island
56 of Sumatra possesses a diurnal cycle pattern comprised of slowly propagating density currents ($3\text{--}5\text{ m s}^{-1}$) and fast

57 propagating gravity waves that extend far offshore (16 m s^{-1}) (Bai et al., 2021; Peatman et al., 2023). Bai et al. (2021)
58 found that this offshore propagation occurs most frequently during MJO phases 1–3, in which WIGs are embedded,
59 and is fastest during boreal summer.

60 It is understood that scale interactions between the diurnal cycle, CCKWs and the MJO, alongside other modes of
61 rainfall variability play a key role in determining local rainfall variability (Wei et al., 2020; Wei et al., 2021; Wei et al., 2021).
62 Despite this, high impact weather events related to CCKWs are often thought of as isolated events. However, scale
63 interactions between the MJO, the diurnal cycle and the WIGs they trigger and, increased convective activity may
64 provide conditions that are conducive for CCKWs to traverse the Maritime Continent and produce extreme weather
65 over a large area, analogous to the propagation of extratropical cyclones in a storm track. While the combined effects
66 of the MJO and the diurnal cycle have been well studied, their separate and combined interactions with CCKWs are
67 less well understood. Furthermore, many prior studies of extreme precipitation linked to the diurnal cycle, equatorial
68 waves and the MJO and their interactions have focused on the boreal winter, since the amplitude and variability of
69 precipitation is greater during this time. However, during the boreal summer, though typically considered the “dry”
70 season and the season in which MJO activity is at its lowest, the MC still experiences precipitation extremes. Since
71 the regional climatology during this period is very different, with southeasterly winds south of the equator turning
72 southwesterly north of the equator, results from analyses of the boreal winter period may not be relevant. Thus a key
73 knowledge gap is not only to understand the processes through which scale interactions of various modes of rainfall
74 variability produce precipitation extremes but those that do in the boreal summer. Here we present such a case study
75 in which a system of CCKWs and diurnally phase-locked WIGs embedded within an active MJO brought extreme
76 precipitation to Sumatra, Borneo and Sulawesi during July 2021 with widespread reports of rainfall-related disasters
77 across these islands.

78 Forecast models, in which convection is parameterised, poorly represent deep convection and the diurnal cycle
79 (Love et al., 2011; Birch et al., 2015) and precipitation intensities associated with key modes of subseasonal rainfall
80 variability (Dias et al., 2018; Menary et al., 2018; Williams et al., 2018; Roberts et al., 2019). In general, models with
81 explicit convection show significant improvements in representing the diurnal cycle and precipitation extremes (Love
82 et al., 2011); however, specifically over the MC where the diurnal cycle is extremely complex across its many islands,
83 mountains and shallow seas, convection-permitting models overestimate the intensity of diurnal precipitation over
84 land compared with gridded (area average) satellite derived observations (Argüeso et al., 2020), but not necessarily
85 when compared with point rain gauge observations (Rowell et al., 2019; Halladay et al., 2023). Convection-permitting
86 models also tend to overestimate the intensity of rainfall associated with mesoscale convective systems (MCSs) and
87 underestimate stratiform rainfall associated with them (Prein et al., 2015; Vincent and Lane, 2018). These MCSs often
88 form and are modulated in the presence of active MJO phases and equatorial waves (Feng et al., 2023; Crook et al.,
89 2024). Though it is difficult to view MCSs as distinct from other equatorial modes in individual case studies. Many
90 convection-permitting forecasts operate within limited area domains and are forced at the boundaries by parame-
91 terised convection models. This may act to reduce the lead time for which the forecast is skillful for rainfall events
92 associated with CCKWs that originate outside the convection-permitting domain (Senior et al., 2023). This case study
93 therefore presents an interesting testbed for assessing the capability of forecast models to predict extreme rainfall
94 events associated with these multiscale interactions.

95 High impact weather events related to CCKWs are often thought of as isolated events. However, scale interac-
96 tions between the MJO, the diurnal cycle and the WIGs they trigger and, increased convective activity may provide
97 conditions that are conducive for CCKWs to traverse the Maritime Continent and produce extreme weather over a
98 large area, analogous to the propagation of extratropical cyclones in a storm track. While the combined effects of
99 the MJO and the diurnal cycle have been well studied, their separate and combined interactions with CCKWs are

100 less well understood. To address this key knowledge gap in how CCKWs may mediate interactions between smaller
101 and larger scale modes of rainfall variability, we study a case in which a system of CCKWs and diurnally phase-locked
102 WIGs embedded within an active MJO brought extreme precipitation to Sumatra, Borneo and Sulawesi during July
103 2021 with widespread reports of rainfall-related disasters across these islands. This case study also serves as an in-
104 teresting testbed for evaluating the ability of forecast models to predict extreme rainfall events associated with these
105 multiscale interactions.

106 The results presented in this paper begin with a description of the convective systems associated with these
107 equatorial modes and their link to high impact weather events across the MC in section 3. We find that during July
108 2021, the MJO was abruptly terminated over the MC by a CCKW after which the MC experienced a pronounced dry
109 period. This is investigated by analysing the total column water and the source terms that influence its changes in
110 section 4. We then examine the role of the diurnal cycle in section 5. Observations of key dynamical fields over west
111 Borneo, one of the worst affected regions during the extreme rainfall events of July 2021, are analysed in section 6.
112 Then the representation of these rainfall events in convection parameterised and convection-permitting determinis-
113 tic Met Office Unified Model (MetUM) configurations are assessed and compared in Section 7. We then provide a
114 discussion on the multiscale scale interactions that occurred between these different modes of rainfall variability and
115 how contributed to the extreme rainfall events of July 2021 (section 8) and highlight the challenges these present for
116 forecast models.

117 2 | DATA AND METHODOLOGY

118 This study uses observations of precipitation rate from the Integrated Multi-satellitE Retrievals for the Global precip-
119 itation measurement mission dataset (IMERG; Huffman et al. (2020)). Daily accumulated rainfall station data, radar
120 (inaRAISE; Permana et al. (2019)) and, zonal wind, temperature and relative humidity data from daily radiosonde as-
121 cents were supplied by the Indonesian Agency for Meteorology, Climatology and Geophysics (BMKG). Reports of high
122 impact weather events related to extreme precipitation were obtained from the ADInet database (ASEAN disaster in-
123 formation network). Wind, total column water, vertically integrated moisture flux and precipitation data are taken
124 from the ERA5 reanalysis dataset (Hersbach et al., 2020). The CCKW trajectory database of Matthews (2021) was
125 used to identify the individual CCKW events during this case study.

126 We examine the performance of four deterministic MetUM simulations for the July 2021 case study. Two dif-
127 ferent global simulations that parameterise convection are run on an N1280 (12 km) resolution grid. One of these
128 utilises version 9 of the Met Office Global Atmosphere and Land model (GAL9). This is the contemporary version of
129 the model based on GA7 Walters et al. (2019) and GA8 (Lock et al., 2024) with updates to the convection scheme. The
130 second global simulation uses an alternative version of the convection scheme, CoMorph-A Lock et al. (2024). We
131 nest two limited area models inside the GAL9 global simulation, both have a 4.4 km grid spacing and 90 vertical levels.
132 We test two different science configurations in the LAM, both explicitly represent deep convection. The first is the
133 operational RAL2T configuration Bush et al. (2023) and the other is the recently released RAL3 science configuration
134 which unifies tropical and mid-latitude science settings in the MetUM. RAL3 differs from RAL2T as it introduces the
135 Cloud AeroSol Interacting Microphysics(CASIM) double-moment cloud microphysics scheme (Field et al., 2023) and
136 uses the bimodal large-scale cloud scheme (Van Weverberg et al., 2021). The LAM models are bounded between 90°E
137 and 154°E and 18°S to 30°N and are forced at the boundaries by GAL9. These were run for 10-days and initialised
138 daily between 6–13 July 2021 at 00:00 UTC.

3 | TIMELINE OF HIGH IMPACT WEATHER EVENTS ACROSS THE MC

During July 2021 several regions across equatorial Indonesia experienced hazardous rainfall extremes. Locations and dates of reports of high impact weather events across Indonesia between 9–17 July related to this weather system are shown in Figure 1. We analyse the spatial and temporal distribution of reports of these weather events across the country, linking them to larger scale weather systems identified in IMERG precipitation and ERA5 850 hPa winds in Figure 2. Between 5–6 July, there were numerous reports of flooding caused by heavy rainfall and rivers overflowing in several northern and western regencies of Aceh, in Northern Sumatra. There was a lull in the rainfall intensity between 7–8 July until a new weather system moved into the MC. The events unfolded as follows:

9 July 2021 The northern Sumatra regencies of Aceh Besar and Aceh Jaya were again inundated with heavy rainfall and floods leading to damage to infrastructure. On this day there was a band of precipitation over the region associated with strong southwesterlies at around 5°N, coinciding with an anticyclonic flow. (Figure 2a).

10 July 2021 These southwesterlies turned westerly and the weather system passed over northern Sumatra (Figure 2b), and further high impact weather events were reported in the north eastern Sumatra regency of Aceh Tamiang.

11 July 2021 A large convective system developed ahead of near-equatorial westerlies between 90–100°E. Separately, the first of a series of high impact weather events related to extreme rainfall in the island of Sulawesi was reported (Figure 2c), due to a separate convective system causing floods and landslides.

12 July 2021 The equatorial westerlies intensified, with a development of cyclonic flow around 7°N and 7°S with northwesterly flow parallel to the west coast of Sumatra and a convective system developing in the Karimata Strait. There were reports of high impact weather in each of the islands of Sumatra, Borneo and Sulawesi (Figure 2d). In the northeastern Sumatra regency of Batu Bara several villages and areas of agricultural land were submerged and there were also floods in central Sulawesi. Later on in the day rainfall intensities increased over the Karimata Strait and a convective system began encroaching on the West Kalimantan province (West Borneo) with the North Kayong regency reporting severe weather, floods and damage to infrastructure. One fatality was recorded in relation to a landslide in this region and around 25,000 people were internally displaced.

13 July 2021 The region of strong westerlies and intense precipitation extended across the Karimata Strait to western Borneo (Figure 2e), and there were reports of floods and landslides related to a high sea state, strong onshore winds and heavy rainfall in the Mempawah regency (north of Pontianak) and widespread flooding in the city of Pontianak itself due to the Kapuas river breaking its banks. Floods of 2 m depth were reported in central Borneo in the regency of Kapuas Hulu. There were also reports of high impact weather in the regency of Bengkulu in south Sumatra, as a component of the convective system traversed Sumatra.

14 July 2021 The convective system led to a strong southwesterly flow, appearing to be deflected by the mountains in central Borneo into the South China Sea (Figure 2f). There were further reports of high impact weather events in Borneo.

15 July 2021 There was an increase of convective activity over the Makassar Strait and the Celebes Sea (Figure 2g). Floods and landslides were reported in the northeastern regions of Sulawesi including the city of Manado. There were also further reports of high impact weather events in Borneo due to several days of continuous rainfall.

16 July 2021 As the convective system, coinciding with westerlies turning to northwesterlies, moved over Sulawesi (Figure 2h), there were widespread reports of high impact weather events across the whole island, with some areas reporting 2 m floods and a 150 m long landslide in Bolaang Mongondow, North Sulawesi.

17 July 2021 As the convective system travelled further eastwards (Figure 2i), there were more reports of floods and

180 landslides in central Borneo and South Sulawesi. After this point the whole of the western MC experienced dry
181 conditions.

182 The convective systems linked to the high impact weather events may be understood by examining the large-scale
183 conditions. Convection over the MC and the eastern Indian Ocean during July 2021 was organised into eastward
184 propagating CCKWs (with trajectories shown in Figure 3a), westward propagating gravity wave-like features related
185 to the diurnal cycle and an active MJO. Several CCKW trajectories have been identified over this period with three
186 notable trajectories that can be related to the high impact weather events identified previously. CCKW-A, the first of
187 these, crossed into Sumatra on 5–6 July. Floods and landslides reported in the Aceh region may be attributed to this
188 CCKW. A convective system can also be seen propagating westwards offshore from the west coast of Sumatra on 4
189 July and coinciding with CCKW-A. Convection off the west coast of Sumatra increases as this combined MCS draws
190 closer to the coast. This interaction and modulation of the diurnal cycle is a key mechanism through which CCKWs
191 may produce rainfall extremes along the west coast of Sumatra (Senior et al., 2023). After CCKW-A passed, there was
192 a period of relatively low precipitation in Sumatra (on 7–8 July) and in west Borneo (on 8–9 July), possibly due to the
193 divergent phase of the CCKW inhibiting convection locally.

194 On 9 July, CCKW-B approached the west coast of Sumatra ~~and crossed into the longitudes of the Karimata Strait~~
195 ~~and terminated there on 10 July. Its trajectory coincided with the reports of high impact weather in the Aceh region~~
196 ~~on these dates.~~ . The trajectory line of CCKW-B, as calculated using wavenumber-frequency filtering, shows CCKW-
197 B terminating shortly before arriving at Sumatra. However, its convective signal appears to extend much further,
198 crossing into the longitudes of the Karimata Strait and terminating there at approximately 00:00 UTC, 11 July. Upon
199 examining Figure 2a and b, an anticyclonic flow over Sumatra can be identified. This flow may have been induced by
200 the westerlies associated with CCKW-A interacting with the background easterlies of the MJO (phase 2). This flow
201 likely acted to deflect CCKW-B northwards and through the strait of Malacca, coinciding with reports of high impact
202 weather events in the Aceh region between 9–10 July. Hence the trajectory calculated using wavenumber-frequency
203 filtering (see section 2), which assumes convective signals associated with CCKWs are located close to the equator
204 (between 2.5°S–2.5°N), did not capture its full passage.

205 CCKW-C was the final of these three CCKWs, which initiated in the Indian Ocean (at 75°E) on 9 July. The convec-
206 tion associated with this CCKW coincided with the convergence of easterly and strong westerly 850 hPa zonal winds.
207 Almost exactly two days after CCKW-B, the trajectory of CCKW-C crossed over Sumatra on 12 July and interacted
208 with a westward propagating disturbance, crossed over the west coast of Borneo on 13 July 2021 and approached the
209 west coast of Sulawesi around 15 July. Intense precipitation along the CCKW trajectory and strong westerly winds
210 (15 m s^{-1}) over Borneo can be seen during this time, coinciding with the reports of severe weather over the West
211 Kalimantan province and East Malaysia over that period. As CCKW-C crossed over Sulawesi between 15–17 July, it
212 appears to have interacted with several packets of strong westward propagating convective systems, which together
213 account for the high impact weather events across the island over this period. CCKW-C then continued eastward to
214 cross the rest of the MC. The passage of this CCKW coincided with an abrupt termination of the convective activity
215 and the MJO over the MC.

216 Between 1–12 July 2021, the MJO phase, as calculated using the RMM1 and RMM2 indices Wheeler and Hendon
217 (2004), was between 2 and 3 (Figure 3b). ~~In Figure 3a, this can be inferred by the intensified convective activity over~~
218 ~~the Indian Ocean between 60–95°E.~~ Though the main convective envelope of the MJO was over the Indian Ocean, it
219 is known that diurnal activity is enhanced over the MC during these phases, ahead of the MJO's arrival (Peatman et al.,
220 2014). The numerous westward propagating convective systems evident in Figure 3a appear strongly linked to the
221 diurnal cycle. ~~These have been~~ Similar features have been identified in previous research as westward propagating

222 inertio-gravity waves and are commonly embedded within the MJO (Nakazawa, 1988; Kiladis et al., 2009; Ruppert
 223 and Zhang, 2019). This can be seen particularly in the average precipitation rate over north-west Sulawesi (lilac line in
 224 Figure 3b) as these waves correspond to pulses of increased precipitation rate which occur at roughly the same time
 225 each day, around 21:00 UTC (e.g., peaks on 8, 10, 11, and 15). The role of WIGs and their link to the diurnal cycle
 226 will be examined later in this paper. **Between 13–19 July, the MJO phase rapidly shifted through phases 3 and 4 into**
 227 **phase 5 (Figure 3b), characterised by suppressed convective activity sweeping eastward over the MC, immediately**
 228 **following the passage of CCKW-C.**

229 4 | ABRUPT TERMINATION OF MJO

230 There was a clear suppression of convective activity after CCKW-C crossed the MC, **coinciding with a rapid shift of**
 231 **the MJO phase from active phase 2, when CCKW-C arrived at Sumatra, to suppressed phase 5, when the CCKW**
 232 **exited the MC.** This is also evident when examining the total column water (M ; Figure 4a).

233 The numerous WIGs are also evident in M as bands of westward propagating regions of increased moisture.
 234 Pulses in the precipitation rate along the trajectory of CCKW-C (Figure 3a) correspond also to regions of increased
 235 M (Figure 4a). These pulses arise when WIGs interact with CCKW-C. On 8 July, there was a significant increase in
 236 M over the city of Pontianak on the west coast of Borneo (Figure 4b). There were peaks of M over Pontianak at
 237 approximately 21:00 UTC on 8, 9, 10, 12 and 15 July. These peaks are likely associated with the diurnally coupled
 238 WIGs (Figure 3a). On 11 July there was a peak at approximately 03:00 UTC associated with an interaction between
 239 the WIG and CCKW-B. On 12–13 July M reached a local maximum following interactions between CCKW-C and
 240 WIGs on 12 and 13 July and there was a pronounced decrease in M on 14 July. **On 15 July there was a small local**
 241 **increase** **Following a small local increase** in M due to another WIG **and**, **there was** a continual decrease in M between
 242 16–19 July **as the MJO shifted into suppressed phase 5.** ERA5 ~~well-represents M~~ **represents M well** when compared
 243 to daily radiosonde ascents at Pontianak (Figure 4b).

244 We investigate the process through which the CCKW-C triggered the widespread drying across the MC **that**
 245 **coincided with an abrupt shift in MJO phase,** by examining the moisture budget given by

$$\frac{dM}{dt} = -\nabla \cdot \mathbf{F} - P + E. \quad (1)$$

246 Here we see that the rate of change of the vertically integrated total column water ~~M~~ dM/dt , is governed by the
 247 divergence of the vertically integrated moisture flux (\mathbf{F}), the precipitation rate (P) and the evaporation rate (E).

248 The convergence of \mathbf{F} shows several peaks associated with CCKWs and WIGs crossing the west coast of Borneo
 249 (Figure 5a). There is convergence associated with the passage of CCKW-B between 06:00 UTC 10 July and 06:00 UTC
 250 11 July as well as sustained convergence on 12 July with peaks where two WIGs cross the west coast of Borneo
 251 at 06:00 UTC and 21:00 UTC. Between 03:00 UTC, 13 July to 09:00 UTC, 14 July there is an intense period of
 252 convergence associated with the combined MCS that resulted from interactions between CCKW-C and the WIGs.
 253 This is then followed by a period of comparatively weaker divergence between 09:00 UTC–21:00 UTC 14 July.

254 P as given by ERA5 (Figure 5a) shows a peak precipitation rate of $0.0006 \text{ kg m}^{-2} (\equiv 2.16 \text{ mm hr}^{-1})$ at 06:00 UTC
 255 13 July that tapers down to near-zero by 00:00 UTC 15 July. This is lower than the amplitude of convergence of \mathbf{F}
 256 and the peak rainfall occurs earlier than the peak convergence. However, there are earlier localised peaks of rainfall,
 257 such as on 10 July, that closely match the amplitude and timing of convergence of \mathbf{F} . P as given by IMERG (Figure 5b)
 258 shows a peak precipitation rate of $0.0014 \text{ kg m s}^{-1} (\equiv 5.06 \text{ mm hr}^{-1})$ at approximately 18:00 UTC on 13 July that

259 reduces significantly by 06:00 UTC on 14 July. The timing of the peak IMERG precipitation rate is different from
260 that given by ERA5 (Figure 5a, occurring instead at a similar time to when there is peak convergence of F , and the
261 amplitude of the peak precipitation rate exceeds that moisture convergence and is more than double that given by
262 ERA5.

263 E is small compared to the other terms in (1) with regular peaks between 00:00 UTC–12:00 UTC corresponding
264 to evaporation through insolation. There is a slight increase in E on 13–14 July due to increased precipitation and
265 high windspeeds during this period.

266 The moisture budget calculated with all source terms in (1) from ERA5 (Figure 5a) does not balance dM/dt . It
267 shows instead a significant moistening of the water column through the convergence of F that is not removed by
268 P . Only when F becomes divergent between 09:00 UTC–21:00 UTC 14 July does the total source match the trend
269 in dM/dt . The moisture budget calculated using divergence of F and E from ERA5, and P from IMERG (Figure 5b)
270 closely resembles the trend in dM/dt , showing sustained drying of the water column during 13 July as well as on 14
271 July.

272 ~~The rate of change M given by ERA5 in the vicinity of Pontianak, is punctuated by high-intensity pulses at~~
273 ~~09:00 UTC and 21:00 UTC. High-intensity pulses at 09:00 UTC and 21:00 UTC punctuate dM/dt in the vicinity of Pon-~~
274 ~~tianak (thick black lines in Figure 5a and Figure 5b. These are the times of the 12 hourly ERA5 data assimilation steps~~
275 ~~(Hersbach et al., 2020). Around the time CCKW-C crosses, between 18:00 UTC, 13 July to 21:00 UTC, 14 July, there~~
276 ~~is a pronounced drying of the water column indicated by the negative rate of change of M .~~ These data assimilation
277 steps appear to compensate for discrepancies in the moisture budget. For example, between the two data assimila-
278 tion steps at 21:00 UTC, 13 July and 09:00 UTC, 14 July, P given by IMERG (Figure 5b) shows greater rainfall rate
279 than P given by ERA5 (Figure 5a). ~~Therefore, M as measured by radiosondes would have demonstrated an increased~~
280 ~~drying compared to that calculated in the ERA5 reanalysis resulting in an adjustment in the data assimilation step. This~~
281 ~~shows that the rainfall over this period was greatly underestimated in ERA5 such that the sum of source terms in the~~
282 ~~moisture budget gives a positive trend in M (thick gray line; Figure 5a). However, the real atmosphere would have~~
283 ~~shown a decrease in M between 21:00 UTC, 13 July and 09:00 UTC, 14 July due to the significant volume of rainfall~~
284 ~~that occurred over this period (IMERG precipitation rate, blue line; Figure 5b). This discrepancy is compensated for~~
285 ~~by decreasing M at the data assimilation step which appears as a spike of negative dM/dt in Figure 5 at 09:00 UTC,~~
286 ~~14 July. This allows for M in ERA5 to closely align with observations despite the erroneous representation of rainfall~~
287 ~~rate. This is why the moisture budget is not self-consistent in ERA5 at a given timestep and is better closed using P~~
288 ~~given by IMERG rather than that given by ERA5.~~

289 We now examine the Hovmöller diagrams of terms in the moisture budget given by (1) over the region. The
290 divergence of F (Figure 6b) shows strong convergence along the trajectories of CCKW-B and CCKW-C, along with
291 notable westward propagating regions of convergence corresponding to WIGs. Following the passage of the CCKW-C
292 and as it enters its westerly phase, there is a period divergence of F that is weaker than the convergence and there is
293 no divergence associated with the CCKW beyond about 120°E. Though there is a background larger-scale divergence
294 in F associated with the shift in MJO ~~phase activity~~.

295 Consistent with the budget analysis at Pontianak, the Hovmöller diagram of the sum of the source terms using P as
296 given by ERA5 (Figure 6c) does not match dM/dt , especially along the trajectory of CCKW-C where the precipitation
297 rate (Figure 6d) is consistently lower than observed by IMERG (Figure 6f). Instead, the ~~weak rainfall in ERA5 rainfall in~~
298 ~~ERA5 is much weaker (Figure 6d) does not exceed compared to the convergence of F (Figure 6b), the moisture budget~~
299 ~~as calculated using ERA5 along CCKW-C closely match hence the moisture budget as calculated using ERA5 over~~
300 ~~CCKW-C is dominated by the convergence of F .~~ Notably, the westward propagating convective systems associated
301 with the WIGs are not identifiable in P from ERA5 (Figure 6d).

302 In contrast, the sum of the source terms obtained using P from IMERG instead of ERA5,(Figure 6e) better resem-
 303 bles the pattern in dM/dt , with a period of sustained drying following the passage of CCKW-C. The intensity of P
 304 given by IMERG (Figure 6f) is often considerably stronger than that given by ERA5 (Figure 6d). Thus, the moisture
 305 removed by P in IMERG is greater than that supplied by the convergence of F over the CCKW trajectory, which leads
 306 to a drying of the water column. The duration of the most intense rainfall in IMERG precipitation is longer compared
 307 to that of ERA5 over the CCKW trajectory. This suggests that the intensity of rainfall over the CCKW trajectory was
 308 the primary driver of the abrupt shift in the MJO phase from phase 2 to phase 5.

309 The magnitude of the drying trend obtained using P from IMERG is actually greater than that calculated from
 310 dM/dt (Figure 5b and Figure 6e) over the transit of CCKW-C. IMERG represented well the precipitation rate over
 311 west Borneo compared to observations (this is discussed in section 6), this suggests that the convergence of F was
 312 also underestimated in ERA5, in addition to the precipitation rate.

313 The rate of change of M as given by ERA5 (Figure 6a) is mostly positive before CCKW-C passes over western
 314 Indonesia. Before CCKW-C passes over western Indonesia, dM/dt as given by ERA5 (Figure 6a) is mostly positive,
 315 suggesting a sustained moistening possibly due to the MJO convergence. After CCKW-C passes, there is a period of
 316 rapid drying particularly over Sumatra and Borneo. There is also large-scale drying over the entire MC as the MJO
 317 shifts to the suppressed phase. The data assimilation steps that were observed as short pulses at 09:00 UTC and
 318 21:00 UTC in line plots of dM/dt (Figure 5) are also seen in the Hovmöller diagram (Figure 6a). We have seen that
 319 the sum of source terms as calculated using ERA5 P closely resembles the patterns in the divergence of F . Since the
 320 divergence of F following the passage of the CCKW, is much weaker than the convergence, this would not have led
 321 to the pronounced drying that is seen in dM/dt (Figure 6a). This confirms what was understood from analysing the
 322 moisture budget at Pontinank, that the strong negative pulses seen in dM/dt after CCKW-C passes, are where data
 323 assimilation steps are compensating for the reanalysis erroneously representing rainfall, which would have otherwise
 324 led to an excess of moisture in the water column compared to observations.

325 5 | ROLE OF DIURNAL CYCLE

326 We have seen that there are WIGs present in the precipitation rate, total column water and vertically integrated
 327 moisture flux divergence, and that these waves tend to occur at approximately the same time of day, exhibiting strong
 328 coupling with the diurnal cycle. Interestingly, each of the three main CCKWs linked to the reported HIW events also
 329 demonstrate overlap with the diurnal cycle, crossing 100°E , i.e. the west coast of Sumatra, around the same time of
 330 day, with pulses of precipitation occurring between 12:00 UTC to 21:00 UTC (black line, Figure 3b). This is consistent
 331 with findings in Senior et al. (2023) (see their Figure 3b and Figure 3c), where the lagged composite precipitation rate
 332 of CCKWs linked to extreme precipitation days in Padang, Sumatra show enhanced precipitation and convergence at
 333 100°E coinciding with the coastal diurnal cycle peak. As CCKW-B crossed Sumatra into the Karimata Strait, it triggered
 334 multiple WIGs. It arrived there (around $105\text{-}110^\circ\text{E}$) at 2100 UTC on 11 July and terminated here, triggering a final
 335 WIG. Each of these WIGs appear to have traveled back westwards over Sumatra and coincided with CCKW-C almost
 336 a day later. For example the final of these WIGs triggered by CCKW-B coincided with CCKW-C around 1800 UTC on
 337 13 July, offshore from the west coast of Sumatra at around $95\text{-}100^\circ\text{E}$. This shows striking similarity to Figure 3b of
 338 (Senior et al., 2023) where a westward propagating convective system is present in the composite analysis of extreme
 339 precipitation CCKWs at these times: at lag $\tau = 24 - 30$, corresponding to the day after CCKW cross the west coast of
 340 Sumatra, there is an increase in precipitation rate at $105\text{-}110^\circ\text{E}$ in these composites.

341 Given that these WIGs appear at similar times of day, we examine the mean diurnal cycle of convection along the

342 equatorial belt (1.5°S - 1.5°N) over the region (Figure 7). The arrangement of land masses and water bodies is such that
343 there is a patchwork of interacting diurnal cycle patterns which in general appear to favour westward propagation.
344 Note that at these latitudes, the island of Sulawesi is comprised of both land and sea components so it is difficult to
345 comment on the diurnal cycle to the east of the Makassar strait.

346 Conditions over the central islands of Sumatra and Borneo are dry when insolation peaks at local midday (\approx
347 05:00 UTC, green-yellow lines in Fig. 7). However, in the surrounding seas there is precipitation at this time of day,
348 peaking in the Karimata Strait and the eastern Indian ocean, and just after the peak in the Makassar Strait. As the
349 afternoon progresses, between 05:00-10:00 UTC, convection increases over the Barisan mountains on the west coast
350 of Sumatra and over the coastal mountains in west Borneo. Convection also propagates onshore from the Karimata
351 Strait, on the east coast of Sumatra and inland over Sumatra. Similarly, convection also propagates westwards in the
352 Makassar Strait and onshore in equatorial Borneo. Precipitation on the west coast of Borneo increases at this time.

353 In the local early evening (\approx 11:00 UTC) conditions on the east coasts of Sumatra and Borneo are relatively dry
354 whilst precipitation increases on the west coast of Sumatra and peaks on the west coast of Borneo. As the evening
355 progresses (between \approx 12:00-15:00 UTC) the offshore land breezes are evident as: a weakening of westerlies on the
356 west coasts of Sumatra and Borneo and strengthening westerlies on the east coast of Sumatra. Precipitation on the
357 west coast of Sumatra peaks and propagates offshore, whilst a lower amplitude component propagates inland from
358 the Barisan mountains on the west coast of Sumatra (see Figure 1. On the west and east coast of Borneo there is
359 also propagation of a convective system towards the centre of the island. At local midnight (\approx 17:00 UTC; purple
360 lines in Figure 7), the convergence of sea breezes over the mountainous region in central Borneo leads to a nocturnal
361 rainfall peak there. Overnight between 17:00–23:00 UTC, the main precipitation envelope over Sumatra and Borneo
362 propagates into the Indian Ocean and Karimata Strait respectively at speeds of $\approx 13 \text{ m s}^{-1}$; this speed is too fast for a
363 land breeze (i.e., density currents with speeds of $\approx 3\text{-}6 \text{ m s}^{-1}$) but consistent with the phase speeds of gravity waves.

364 Gravity waves and density currents are both mechanisms that contribute to the diurnal cycle of precipitation in
365 Sumatra, Borneo and Sulawesi (Bai et al., 2021; Peatman et al., 2023). Where as density currents are more localised,
366 gravity waves travel much further and are longer lived. The arrangement of land-masses in the equatorial MC may be
367 conducive to gravity wave propagation. The diurnal peaks of convection in the Makassar Strait and Karimata Strait
368 are close enough to the coastlines to experience the late morning sea breeze. Though the gravity waves travel con-
369 siderably faster than the mean winds, the sea breezes may provide favourable conditions for the waves to propagate
370 onshore towards the central island and mountainous regions. In the afternoon, these gravity waves then contribute
371 to the development of convection over the Barisan mountains on the west coast of Sumatra and then experience
372 the coastal land breezes during the late evening. In theory, triggered gravity waves may travel in any direction. How-
373 ever, between the islands of Borneo and Sumatra and to some extent between Sulawesi and Borneo, the westward
374 propagating component appears to be favoured over the eastward. The presence of WIGs is a common occurrence
375 during active MJOs (Kiladis et al., 2009; Ruppert and Zhang, 2019). Though all MJO phases have been included in
376 this composite, active MJO events are likely to account for a significant portion of these events since they enhance
377 diurnal activity, therefore leading to enhanced WIG activity. Furthermore, CCKW activity also increases during MJO
378 events, though they are less frequent, they may account for some of the eastward propagation seen in the composite
379 diurnal cycle in addition to eastward propagating inertio-gravity waves.

6 | OBSERVATIONS OF EXTREME RAINFALL IN PONTIANAK AND WEST KALIMANTAN

A convective system driven by CCKW-C traveled across the MC with a particularly strong intensity over the city of Pontianak and the West Kalimantan province (Borneo) on 13–14 July 2021. The rainfall associated with CCKW-C was particularly intense over the city of Pontianak and the West Kalimantan province (Borneo) between 13–14 July 2021. We will now examine the rainfall properties and CCKW structure using in situ data from the region. This allows us to validate the representation of the processes in IMERG and ERA5, as well as examine the shift in atmospheric conditions following the passage of CCKW-C.

Many stations in the West Kalimantan region recorded heavy (>50 mm) to extreme (>150 mm) rainfall accumulation on 13 July (Figure 8), with a maximum recorded accumulated rainfall of 370 mm in the Mempawah region (not shown). The daily accumulated rainfall pattern, as estimated by C-band Doppler radar, revealed the intense convective system that traveled from the east and passed over the West Kalimantan province, with particularly high amplitudes (80–140 mm) over the western coastal regions on 13 July (Figure 9). The peak rainfall given by IMERG on 13 July, 2021 in the vicinity of Pontianak was 5.1 mm hr^{-1} (121 mm day^{-1}) which agrees well with the station and radar data.

We examine radiosonde ascents at two locations to understand how the vertical structure of CCKW-C developed as it crossed the western MC. The first radiosonde ascent is at Padang (Figure 10a), a city on the equatorial west coast of Sumatra, and the second is at Pontianak (Figure 10b). These cities are approximately 10° longitude apart, which is approximately the distance a CCKW travels in a day. CCKW-B crossed Padang at approximately 18:00 UTC on 9 July. Following this on 10 July, a low-level westerly wind signal can be seen as the westerly phase of this CCKW follows. CCKW-C, which brought extreme rainfall to Pontianak, crossed Padang at approximately 12:00 UTC on 12 July. Following this, on 13 July, the winds at around 800–850 hPa became stronger and the westerly signal increased in height as time progressed. CCKWs are known to have structures that tilt westward with height (Kiladis et al., 2009), so as this structure moves towards the east, this should manifest as an increase in height with time.

To understand how the vertical structure of CCKW-C developed as it crossed over the western MC, we examine daily radiosonde ascents of zonal wind at Pontianak (Figure 10a) and at Padang (Figure 10b), a city on the equatorial west coast of Sumatra that lies about 10° west of Pontianak. This is approximately the distance a CCKW travels in a day. Note that radiosonde observations are taken at 00:00 UTC

The radiosonde measurements at Padang show a weak low-level westerly wind signal on 12 July (Figure 10b). By 13 July the winds at around 800–850 hPa have become stronger and the westerly signal is increasing with height. This is consistent with the presence of CCKW-C, since its trajectory (associated with its convergent phase) crossed Padang at approximately 12:00 UTC on 12 July. CCKWs are known to have structures that tilt westward with height (Kiladis et al., 2009), so as the CCKW progressed eastwards, this manifested as an increase in height with time.

At Pontianak (Figure 10b) surface-level westerlies are observed on 11 July, shortly after CCKW-B arrives. There is a rapid increase in intensity of these westerlies from 6 ms^{-1} up to 15 ms^{-1} on 14 July. This is consistent with the low-level convergent phase of the CCKW arriving at Pontianak on 13 July. After this point, the westerlies increase with height similarly to what was observed at Padang a day earlier. Indeed, the patterns of the zonal wind measured by radiosonde ascents at Padang (Figure 10a) and Pontianak (Figure 10b) are similar, except shifted a day later at Pontianak.

At Pontianak (Figure 10a) weak surface-level westerlies are observed on 11 July. The intensity of these westerlies increases rapidly between 13 July (6 ms^{-1}) to 14 July (15 ms^{-1}). This is consistent with the convergent phase of CCKW-C arriving at Pontianak on 13 July. By 15 July, the westerlies have increased with height. In general, the strong westerly wind pattern measured by radiosonde ascents at Pontianak (Figure 10a) is similar to that at Padang

422 (Figure 10b), but appear to be shifted by a day.

423 For comparison, we examine the longitude-height section of ERA5 zonal wind anomaly at Pontianak on 13 July
424 in Figure 11. The convergent region of CCKW-C, which crossed Pontianak on 13 July, can be seen as a switch from
425 low-level anomalous easterlies to westerlies at approximately 110°E. These westerly winds tilt westward with height,
426 as inferred from the radiosonde data (Figure 10).

427 We now investigate the potential temperature and relative humidity associated with the CCKW envelopes as
428 measured by radiosonde ascents at Pontianak. These are characterised by distinct regions of moistening and drying
429 as each CCKW passes. On 8 July there was an increase in low-level humidity associated with CCKW-A (Figure 12a).
430 There was a period of relative heating and drying as the divergent phase of the CCKW passed, which corresponded
431 to a period of suppressed precipitation over this time. After this there was a build up of low level moisture on 10 July.
432 On 11 July, the entire tropospheric column at Pontianak exhibited high relative humidity, associated with the deep
433 convection of CCKW-B. This was followed by a short period of relative drying on 12-13 July before the troposphere
434 was once again moistened throughout the column on 14 July, associated with the deep convection within CCKW-
435 C. On 14 July, there was pronounced drying of the lower troposphere, presumably due to descent of dry air in the
436 suppressed phase of the CCKW after its active region had passed through Pontianak. ~~This is associated with the~~
437 ~~shift in the MJO into the suppressed phase.~~ This is associated with the shift in the MJO conditions, from active into
438 suppressed.

439 The potential temperature field also demonstrates these CCKW signals (Figure 12b). On 8 July there is a remnant
440 cooling over the tropospheric column as CCKW-A passed Pontianak. On 11 July, the entire lower troposphere cools
441 diabatically relative to 10 July due to evaporation following intense rainfall. On 12 and 13 July, the potential tempera-
442 ture of the lower troposphere recovers, before once again cooling on 14 July after the peak in convection associated
443 with CCKW-C. There is a demonstrable shift in atmospheric conditions after the CCKW-C passes. The very dry region
444 below 750 hPa on 15 July is coincident with significantly higher potential temperatures, whereby dry, descending air
445 leads to a positive temperature perturbation.

446 7 | REPRESENTATION IN FORECAST MODELS

447 We have examined how different convective processes brought extreme precipitation to equatorial Indonesia during
448 July 2021. We now assess different deterministic MetUM model configurations and evaluate the representation of
449 the extreme precipitation event in the West Kalimantan region and the ~~post-event drying~~ shift to suppressed MJO
450 conditions following the passage of CCKW-C.

451 7.1 | Parameterised convection (CoMorph A and GAL9)

452 First we examine Hovmöller diagrams of two deterministic global models with parameterised convection, one us-
453 ing GAL9 and the other using the CoMorph A convection scheme built on top of GAL9. In observations (IMERG,
454 Figure 3a), CCKW-C initiates around 9 July 2021 in the Indian Ocean so this CCKW is present within the initial con-
455 ditions of these model simulations. Both models simulate an organised region of eastward propagating convection
456 associated with westerly 850 hPa zonal winds, consistent with the presence of CCKW-C. When initialised on 9 July
457 2021 (Figure 13a), CoMorph A shows a strengthening of the westerly winds near the west coast of Borneo and an in-
458 crease of precipitation here on 13 July. In CoMorph A this results in a peak precipitation rate on 13 July over Pontianak
459 at around 18:00 UTC, in line with observations, though the amplitude of precipitation is much lower (Figure 13e). In

460 GAL9 (Figure 13b) there are weaker winds and precipitation compared to CoMorph A and the peak precipitation at
461 Pontianak occurs on 12 July 2021, a day earlier than observed (Figure 13e). On 9 July 2021 CCKW-B traversed
462 across Sumatra into the Karimata Strait and coincided with a WIG. When these models are initialised on 9 July 2021
463 at 00:00 UTC (Figure 13a and b respectively), they should contain CCKW-B within their initial conditions. However,
464 in both CoMorph-A and GAL9, the presence of CCKW-B is not distinguishable and the WIG is largely absent. The
465 CoMorph A scheme has been found previously to show a poorer representation of gravity waves in idealised island
466 experiments compared to GAL8 Lavender et al. (2024). This is also evident for this case study where the diurnally
467 phase-locked WIGs in general are poorly represented in CoMorph A at all initialisation times (Figure 13a, f and k), ap-
468 pearing more as patchy regions of convection. In contrast, GAL9 configurations are better able to represent WIG-like
469 propagation (Figure 13b, g and l).

470 The representation of the precipitation rate at Pontianak on 13 July 2021 CoMorph A and GAL9 generally im-
471 proves with later initialisation times. When CoMorph A and GAL9 are initialised on 11 July 2021 at 00:00 UTC
472 (Figure 13f and g respectively). Both models simulate a peak of intense precipitation between 12–13 July (Figure 13j).
473 When the models are initialised on 13 July 2021 at 00:00 UTC (CoMorph A and GAL9, Figure 13k and l respectively)
474 the precipitation rate at Pontianak (Figure 13o) is well represented, as expected given the short lead time.

475 7.2 | Convection-permitting (RAL2T and RAL3)

476 We now assess the representation of the convective processes identified in 4.4km resolution simulations using two
477 regional configurations, RAL2T and RAL3, of the MetUM. Both regional models are forced at the lateral boundaries
478 by GAL9. Note that the full longitudinal domain for these models are shown, with the eastern boundary at 90°E and
479 the western boundary at 154°E.

480 When the regional models are initialised on 9 July 2021 at 00:00 UTC (Figure 13c and d respectively), CCKW-
481 B is not present in the initial conditions though it is present at this time in observations. This is due to its weak
482 representation in the global forcing GAL9 model (Figure 13b).

483 In both models, precipitation associated with CCKW-C is weak west of 120°E compared to observations, ap-
484 pearing more as a strengthening of the precipitation rate when WIGs cross its trajectory and the point at which the
485 propagation of the WIGs terminates. Though the convection associated with CCKW-C is weak in the models, the
486 westerly winds associated with CCKW-C are present, so it is possible that the low-level divergent phase of the CCKW
487 is better represented than the convergent phase, resulting in the inhibition of convective activity at this point. How-
488 ever, east of 120°E the convection associated with CCKW-C is more coherent, represented as a sustained eastward
489 propagating convective system along the trajectory of CCKW-C in both models. This appears to be tightly coupled to
490 the gradient in 850 hPa zonal wind. The post-event drying is evident in both models, with precipitation rates across
491 the MC strongly decreasing as the westerly winds associated with CCKW-C strengthen.

492 The RAL2T and RAL3 models (Figure 13c and d) simulate several WIG-like systems but they are more numerous
493 and weaker than in observations. The WIGs do not all appear to be phase-locked with the diurnal cycle. Strong WIGs
494 were observed emanating from the eastern MC on 15 July and 17 July (IMERG, Figure 3a). In RAL2T and RAL3,
495 these appear initially as strong daily convective systems but the westward propagation is increasingly stunted as time
496 progresses and is eventually confined to the eastern boundaries by 17 July.

497 The RAL2T and RAL3 models (Figure 13c and d) differ in how the interactions between WIGs and the CCKWs are
498 represented. In observations, there was a local peak of precipitation associated with the interaction between CCKW-B
499 and a WIG initiating on the west coast of Borneo and the Karimata Strait on 10 July at 21:00 UTC (IMERG, Figure 3a).
500 In both models, there is a peak present at this time due to the presence of the WIG, despite the poor representation

501 of CCKW-B. However, since precipitation rates in RAL2T are known to be stronger than in RAL3; this results in a
502 stronger precipitation peak. Furthermore, in RAL2T, this local diurnal peak forms part of a WIG that propagates over
503 the Karimata Strait towards Sumatra, as seen in observations, but this feature is absent in RAL3.

504 Similarly to the parameterised convection models, both RAL2T and RAL3 show an increased precipitation rate
505 in the vicinity of Pontianak on 12 July at 21:00 UTC, 24 hours earlier than in observations (Figure 13e). This rainfall
506 peak is associated with a WIG. A WIG is also present on this day in observations; however, it crosses the west coast
507 of Borneo at 12:00 UTC. What is also missing from both RAL2T and RAL3 is the MCS in the Karimata Strait that
508 developed at around 00:00 UTC on 13 July. The MCS formed as a result of an interaction between the WIG and
509 CCKW-C (Figure 3a). This interaction does not seem to be present in these models. This could be due to CCKW-C
510 being simulated to arrive at West Borneo too early.

511 When the RAL2T and RAL3 models are initialised on 11 July 2021 at 00:00 UTC, CCKW-C is in the vicinity of the
512 western boundary of both models (Figure 13h and i). There is an improvement in how the CCKW and its interactions
513 with the WIGs is represented west of 120°E compared with models initialised on 9 July 2021. This appears as a
514 combined MCS-like system in both models with sustained precipitation as the CCKW approaches Borneo. However
515 these interactions occur in the models a day earlier than observed so both RAL2T and RAL3 still forecast a maximum
516 precipitation rate a day early on 12 July at around 21:00 UTC in the vicinity of Pontianak. This appears tightly coupled
517 to the onset of westerly 850 hPa zonal winds.

518 Curiously, when compared to those initialised 2 days prior (Figure 13c and d), both RAL2T and RAL3 initialised
519 on 11 July (Figure 13h and i) show a worse representation of the post-event drying with no significant decrease in
520 rainfall over the eastern MC. In both models, convection associated with CCKW-C, to the east of 120°E does not
521 appear distinct from the background convective activity. From analysing the moisture budget we have seen that the
522 intense precipitation that occurred over the entire trajectory of CCKW-C as it crossed the MC was responsible for the
523 large-scale post-event drying. However, in both models, but particularly RAL3, CCKW-C does not appear to traverse
524 the MC past the west coast of Borneo. The strength of the westerly winds associated with the CCKW are weak
525 in RAL2T and absent in RAL3 compared to GAL9 east of 120°E. We have seen that the strengthening of westerly
526 850 hPa zonal wind and precipitation in these models appear to be tightly coupled, so in the absence of such winds
527 this also may have contributed to the erroneous termination of the CCKW which would have otherwise triggered the
528 post-event drying.

529 When RAL2T and RAL3 are initialised on 13 July 2021 at 00:00 UTC, precipitation in the vicinity of Pontianak is
530 well represented (Figure 13o). Beyond 120°E, the westerly winds are stronger in both models (Figure 13m and n), the
531 precipitation rate over the CCKW trajectory is sustained and the post-event drying is well captured. However, though
532 CCKW-C appears to traverse the MC, the precipitation rate is not as strong as in observations over its trajectory. This
533 may be because the strong WIG that interacts with the CCKWs are poorly represented in the models. This will be
534 explored in the discussion.

535 8 | DISCUSSION

536 8.1 | Multiscale interactions

537 During MJO phase 2 and 3, diurnal activity is known to be enhanced ahead of the arrival of the main convective enve-
538 lope associated with the MJO and the probability of extreme precipitation is known to increase (Peatman et al., 2014;
539 Da Silva and Matthews, 2021). We have seen that this was the case during the July 2021 extreme precipitation case
540 study presented here. However, missing from previous works is the role of CCKWs and other equatorial waves, which

541 may act to mediate the interactions between the MJO and the local diurnal cycle. Here we will discuss how these
542 convective systems interacted with each other and how these interactions contributed to the high impact weather
543 events reported during July 2021.

544 CCKWs are common subscale features of the active MJO envelope, which organise convective activity. This is
545 evident here from Figure 3a in which several CCKWs with distinctive eastward propagating bands of convection were
546 identified. All instances of extreme precipitation and high impact weather reported during July 2021 in Sumatra, and
547 the majority of those in the rest of the equatorial MC, could be linked to the increased precipitation in the presence
548 of these CCKWs. This corroborates findings in Baranowski et al. (2020) where it was found that CCKWs were present
549 in all MJO-attributed floods in Sumatra and thus CCKWs, rather than the MJO events, were found to be the primary
550 dynamical predictor of precipitation extremes in Sumatra. So whilst the MJO provides favourable atmospheric con-
551 ditions for convective activity, it seems that CCKWs and other equatorial waves could be pivotal for organising this
552 convective activity and producing the precipitation extremes that are observed during active MJO events.

553 Precipitation extremes associated with the MJO are known to manifest as intensified diurnal activity over the
554 MC (Da Silva and Matthews, 2021). During July 2021, the high impact weather events that did not involve CCKWs, in
555 Borneo and Sulawesi, instead involved WIGs linked to the diurnal cycle. These WIGs are often present during active
556 MJO events (Nakazawa, 1988; Takayabu, 1994; Kiladis et al., 2009). They are also found to be strongly diurnally
557 phase-locked in that their convective phase overlaps with that of the diurnal cycles of convection between Borneo and
558 Sumatra (Ruppert and Zhang, 2019), though they travel considerably faster than the diurnal density currents (Peatman
559 et al., 2023). Numerous such diurnally phase-locked WIGs were observed in this case study, with particularly strong
560 WIG convective activity also originating from the Pacific.

561 CCKWs may also demonstrate diurnal phase-locking that increases the precipitation amplitudes associated with
562 them (Baranowski et al., 2016; Senior et al., 2023). The trajectories of all three CCKWs during the July 2021 case
563 study coincided with reports of high impact weather and all arrived at Sumatra in phase with the diurnal cycle. The
564 CCKWs and WIGs travelled at similar phase-speeds but in opposite directions. The interactions between CCKW-C
565 and the WIGs during July 2021 appeared as pulses of moisture flux convergence and increased precipitation rates.
566 The presence of WIGs may have allowed for the CCKWs themselves to become coupled since some WIGs may
567 have been generated by the CCKWs themselves (e.g. through the mechanism described in Liebmann et al. (1997)).
568 From examining the Hovmöller diagrams of precipitation rate (Figure 3a) and convergence of F (Figure 6d), it appears
569 that CCKW-B interacted with the local diurnal cycle of convection on 9 July, and triggered several WIG packets
570 along its trajectory: the first on the east coast of Sumatra, the second on the west coast of Sumatra and the third
571 most prominent one just offshore from the west coast of Borneo. All three of these WIGs interacted with CCKW-C
572 the following day. Several other WIGs originating from Sulawesi, also in phase with the diurnal cycle over Borneo,
573 interacted with CCKW-C producing the intense rainfall over the west coast of Borneo. CCKW-C continued to interact
574 with strong WIGs originating from the Pacific as it traversed the rest of the MC. Thus the WIGs were pivotal in
575 sustaining CCKW-C and causing the observed precipitation extremes associated with its trajectory as it traversed the
576 MC.

577 We find then that the active MJO an active MJO in phases 2–4 provided favourable atmospheric conditions
578 for convection through increased moisture which can be seen as an increase in M (Figure 4) and a general positive
579 rate of change of M over the region (Figure 6a). The diurnal cycle of rainfall was enhanced, which in turn led to
580 the excitement of gravity-waves. Possibly due to the large-scale easterly phase of the MJO, westward propagating
581 waves were favoured. CCKW-A and CCKW-B arrived in phase with the diurnal cycle triggering local precipitation
582 extremes in Sumatra but did not traverse the MC. CCKW-B triggered several WIGs, which in turn interacted with
583 CCKW-C. CCKW-C encountered several other WIGs over Borneo and Sulawesi. It appears then that CCKW-C was

584 fueled by these WIGs, through additional moisture flux convergence leading to intense rainfall observed over the
585 CCKW trajectory. This intense heavy rainfall over the CCKW trajectory significantly reduced the total column water,
586 shifting the atmospheric conditions and. This resulted in an abrupt local termination of the active MJO event— with
587 MJO phase shifting rapidly from active phase 2 to suppressed phase 5 as CCKW-C progressed over the western MC.

588 Results from four MetUM deterministic model configurations also demonstrate a link between CCKW-C and
589 the abrupt shift in convective activity following its passage. All forecasts with parameterised convection showed
590 sustained rainfall over the trajectory of CCKW-C and a suppression of rainfall activity following the passage of CCKW-
591 C (Figure 13). However, in some convection-permitting forecasts, specifically those initialised on 11 July (Figure 13h
592 and 13i), CCKW-C appeared to terminate in the middle of the MC and rainfall over the region remained significant.
593 In contrast, all convection-permitting forecasts initialised on 9 July (Figure 13c and 13d) and 13 July (Figure 13m and
594 13n) demonstrated sustained rainfall over the path of CCKW-C and the CCKW did not terminate over the MC. In
595 these latter forecasts there was a more significant reduction in rainfall activity over the western MC compared with
596 the forecasts with the earlier CCKW termination. These results are further examined in section 8.2.

597 Other mechanisms that may contribute to shifts in MJO conditions include land-surface feedbacks. In this par-
598 ticular case the evaporation rate was consistently low compared to the rainfall rate over CCKW-C (Figure 5) and the
599 rainfall rate was sustained both over land and sea. This indicates that land-surface feedbacks were not a primary driver.
600 Differences in sea surface temperatures (SST) between the MC and the relatively cooler surrounding oceans may have
601 also contributed to the termination of the active MJO event. The models presented in this paper are atmosphere-land
602 only configurations in which SSTs are held constant. These generally demonstrated a marked decrease in convective
603 activity following the passage of CCKW-C. So, though the real-world SST difference may have contributed to the
604 observed shift in MJO conditions, these results from the forecast models suggest that this mechanism was unlikely
605 to have been important.

606 There has been much speculation and debate in the literature about the nature of MJO termination events over
607 the MC Inness and Slingo (2006); Kim et al. (2016); Zhang and Ling (2017); Abhik et al. (2023). This case study high-
608 lights a mechanism through which such events may occur, in which sub-MJO-scale CCKW and WIG modes organise
609 the low-level moisture and interactions between them result in an increase of rainfall that removes moisture from
610 the water column and terminates the MJO propagation. Since WIGs and CCKWs are both common subscale features
611 of the MJO, it is possible that this is not an isolated case. Future works will examine the frequency of MJO events
612 terminated over the MC in this way. The thermodynamic mechanisms of the post-event drying could also be explored
613 further by evaluating changes to the moist static energy budget.

614 8.2 | Challenges in modelling

615 In section 7 the representation of the extreme precipitation event in West Kalimantan, associated with CCKW-C, was
616 examined in four MetUM deterministic model configurations, namely CoMorph A and GAL9 (parameterised convec-
617 tion, global) and, RAL2T and RAL3 (convection-permitting, LAM). Interestingly, models with parameterised convection
618 were able to forecast the extreme precipitation as well as or better than the explicit convection models. The post-
619 event drying was also better captured in the parameterised convection models. Here, we will suggest a number of
620 factors that may have influenced this result.

621 Interactions between the CCKW-C, the diurnal cycle and, diurnally phase-locked WIGs, produced significant
622 amounts of rainfall over West Kalimantan, between 13–14 July. These interactions manifested as pulses of precipitation
623 along the trajectory of CCKW-C. In observations, the convection associated with both systems was distinct relative
624 to the background precipitation. These were pivotal interactions between the CCKW, diurnal cycle and diurnally

625 ~~phase-locked WIGs, which caused significant amounts of rainfall over the region. However, these interactions were~~
626 ~~not represented in many of the models several model runs failed to represent these interactions.~~ As discussed in
627 Senior et al. (2023), CCKWs ~~interact with~~ modulate the diurnal cycle to produce rainfall extremes in two ways: first
628 by enhancing the diurnal cycle of convection through providing additional moisture and convergence, and second by
629 displacing the combined convergence line closer to the coast as the CCKW propagates eastward. ~~These interactions~~
630 ~~in this case study led to the development of several MCSs over the trajectory of CCKW-C, particularly evident In~~
631 ~~this case study, the CCKW-diurnal cycle interaction led to the development of a combined MCS system as CCKW-C~~
632 ~~traversed over the Karimata Strait and west Borneo on 13 July 2021 (Figure 2e). Furthermore, interactions between~~
633 ~~CCKW-C and several WIGs resulted in local increases in rainfall intensity over West Kalimantan, appearing as pulses~~
634 ~~of precipitation in Figure 3a. Model performance was dependent on how the pulses of precipitation and the develop-~~
635 ~~ment of the MCS associated with the interactions between the WIGs and CCKW-C were represented.~~

636 The CoMorph A configuration was the only forecast initialised on 9 July, that captured the rainfall peak in the
637 vicinity of Pontianak on 14 July, as observed (Figure 13a and e). ~~This may be because it represented the timing of~~
638 ~~individual pulses and their combined interactions relatively well.~~ This forecast showed sustained precipitation in the
639 vicinity of Pontianak associated with the development of the MCS as well as pulses of precipitation rate associated
640 with interactions between CCKW-C and the WIGs. Notably, this forecast demonstrated a strengthening of westerly
641 winds associated with CCKW-C over the Karimata Strait on 14 July. This was weaker in the other forecast models. In
642 GAL9 (Figure 13b), convection associated with CCKW-C and the WIGS were present, but the pulses of precipitation
643 associated with their combined interaction were absent, resulting in a forecast showing low but sustained precipitation
644 from around 12 July. The representation of these interactions improved in GAL9 when the forecast was initialised on
645 11 July. The RAL2T and RAL3 forecasts initialised on 9 July, showed a peak of precipitation on 12 July (Figure 13e).
646 This peak could be attributed to the interaction between CCKW-C and the WIGs, appearing as a pulse of precipitation
647 in the vicinity of Pontianak on 12 July. However, the precipitation over the region was not sustained, suggesting
648 that the MCS was not as well represented in these models possibly due to the weak representation of CCKW-C.
649 When these models were initialised 2 days later on 11 July (Figure 13h and i), there was more sustained MCS-like
650 precipitation and a stronger peak precipitation amplitude, as the representation of the convection associated with
651 CCKW-C was stronger. Though the peak precipitation was still forecast to occur a day earlier than observed. ~~However,~~
652 ~~the combined interactions were not well represented and the RAL2T and RAL3 models did not forecast significant~~
653 ~~rainfall in the vicinity of Pontianak(Figure 13e).~~

654 ~~When models were initialised on 11 July, the CoMorph A and GAL9 schemes represented the timing of the~~
655 ~~interactions between the CCKW-C and WIGs, with rainfall peaking on 13 July as observed (Figure 13f and g). All~~
656 ~~other model configurations (Figure 13h and i) represented the interaction of the WIGs and CCKW-C on 12 July that~~
657 ~~produced an extreme rainfall peak on this day (Figure 13j).~~

658 These results show that the CoMorph A scheme and GAL9 configuration better represented the development of
659 the MCS and timing of the peak precipitation associated with the extreme precipitation event between 13–14 July
660 2021, compared to the convection permitting, RAL2T and RAL3 forecasts. During the spin-up for these forecasts,
661 which is around 6–18 hrs for the SEA domain (Short and Petch, 2022), the models had to resolve a number of interac-
662 tions between the CCKW and the WIGs: There were strong interactions observed between the WIG and the CCKW
663 offshore from Sumatra at 90°E and a WIG was triggered off the west coast of Borneo that traveled over Sumatra
664 to interact with the CCKW the following day (Figure 3a). It is possible then that the convection permitting models were
665 less able to resolve these distinct systems during their spin-up, since they occurred close to the model boundaries.

666 Convection-permitting models are known to have a propensity to favour isolated cells of deep convection over
667 larger areas of stratiform rainfall. ~~Whereas, models with parameterised convection favour more widespread shallow~~

668 convection or stratiform rainfall. It is also possible that this is a factor in determining why the models with parame-
669 terised convection better represented the interactions, since the convection associated with each mode was repre-
670 sented to occur over a wider area, which increased the chance that these models captured interactions between the
671 CCKWs and WIGs. Furthermore, intense cells of deep convection in the models with explicit convection may have
672 triggered WIGs in addition to those triggered by the diurnal cycle, resulting in more numerous westward trajectories
673 seen in the forecasts compared to what was observed and what was represented in the forecasts with parameterised
674 convection. This would affect the timing and amplitude of their interactions with the CCKW.

675 ~~The representation of the post-event drying was poorer for the convection-permitting models initialised on 11~~
676 ~~July compared with those initialised on 9 July. The representation in the shift in the MJO conditions, from active~~
677 ~~to suppressed following the passage of CCKW-C, was well represented in all model configurations initialised on 9~~
678 ~~July. This can be seen as a period of suppressed precipitation from 15 July onwards in the vicinity of Pontianak~~
679 ~~(Figure 13e) as well as a general decrease in convective activity following the trajectory of CCKW-C (Figure 13a, b, c~~
680 ~~and d). However, the representation of this post-event drying deteriorated when the RAL2T and RAL3 forecasts were~~
681 ~~initialised two days later on 11 July, with convective activity still evident after 15 July (Figure 13j). The convection~~
682 ~~associated with CCKW-C did not traverse past 120°E in the forecasts initialised on 11 July. The reason for this~~
683 ~~could be that these models showed CCKW-C weakening as it traversed across the MC, compared to observations~~
684 ~~where CCKW-C was associated with heavy rainfall through out its passage.. This is particularly evident in RAL3~~
685 ~~(Figure 13i) where there is no distinctive westerly wind signal beyond 120°E. On 15 July (Figure 2g), the observed~~
686 ~~CCKW travelled northwards into the South China Sea and appeared to decrease in strength, with westerlies decreasing~~
687 ~~in amplitude and the convection was weaker. It then increased in amplitude again after coinciding with several WIGs~~
688 ~~and strong convection in the Strait of Makassar and north of Sulawesi. However, this diurnal activity over Sulawesi~~
689 ~~and surrounding seas appeared more suppressed in RAL2T and RAL3 over 13–14 July, which may resulted in CCKW-C~~
690 ~~halting over this region.~~

691 ~~Furthermore, there~~ There were errors in the representation of the WIGs that originate in the Pacific at the eastern
692 boundary of the regional models. The absence of the interaction between the CCKW and these strong WIGs may have
693 ~~then also~~ contributed to this poor representation of the rainfall over the CCKW trajectory. Hence, the post-event dry-
694 ing and the shift in atmospheric conditions following the passage of CCKW-C were poorly represented in these models.
695 ~~It will be useful therefore in the future to assess the representation of these processes in contemporary pan-tropical~~
696 ~~and global convection-permitting models:~~ Senior et al. (2023) found that extending the convection-permitting domain
697 over the Indian Ocean improved the representation of CCKW forecasts over the MC, it would be useful in the future to
698 assess the representation of these processes in contemporary pan-tropical and global convection-permitting models.

699 The resolution of the of the RAL3 and RAL2T convection permitting forecasts (4.4 km) is not necessarily the
700 scale at which convective processes such as turbulence and cloud formation, are fully numerically resolved. This may
701 necessitate the inclusion of some convection parameterisation at these scales (Honnert et al., 2020; Tomassini et al.,
702 2023). Work is underway to further enhance the capability of the CoMorph scheme such that it is 'scale aware', where
703 convection is selectively parameterised between 1–5 km resolution (Lavender et al., 2024). This may result in forecasts
704 possessing more realistic convective structures and organisation which in turn would lead to better representation of
705 the propagation of tropical waves.

9 | CONCLUSION

A case study has been presented of a series of high impact weather events reported over equatorial Indonesia during July 2021. There were several interacting modes of rainfall variability that were linked to these events: a system of CCKWs, WIGs, and an active MJO event. Their combined multiscale interactions lead to flooding events that could be traced through Sumatra, Borneo and Sulawesi. ~~The MJO event was abruptly terminated following the passage of the final CCKW of the system in which there was a large amplitude of rainfall throughout its trajectory. CCKW-C, the final CCKW in the system, delivered a large volume of rainfall over its trajectory. This CCKW alone accounted , alone accounting for over half of the high impact weather events reported across the region. As CCKW-C travelled across the western MC, the MJO phase rapidly shifted from active phase 2 to suppressed phase 5, characterised by suppressed convection and a drying of the water column in this region.~~

WIGs were found to be strongly phase-locked with the diurnal cycle. The interaction of WIGs and CCKW-C appeared as pulses of precipitation rate (Figure 3) and total column water (Figure 4). Several such pulses were observed over the west Borneo region including the city of Pontianak during an extreme rainfall event on 13 July associated with CCKW-C. It is proposed then that WIGs and CCKWs organised the MJO convection downscale and the WIGs acted to fuel the traversal of CCKW over the MC and contributed to the high rainfall rates recorded over its trajectory. ~~Through examining the terms that contribute to the rate of change of total column water, it was found that the rainfall rate over the CCKW trajectory exceeded the moisture flux convergence provided by the interaction between CCKW-C and the WIGs.~~ This significant rainfall over the CCKW trajectory led to a pronounced drying of the water column that triggered the subsequent termination of the MJO convection.

~~The total column water in ERA5 itself agreed well with that obtained from radiosonde observations at Pontianak, however the amplitude of ERA5 precipitation rate was weak compared to IMERG and hence would not have produced the observed drying of the water column between 13–14 July in Pontianak. This resulted in the rate of change of total column water calculated from ERA5 being dominated by sharp intense spikes at the ERA5 data assimilation steps, where the reanalysis compensated for this discrepancy. Furthermore, it was found that the moisture budget was better closed using the IMERG precipitation rate instead of ERA5.~~

During events like this, in which the equatorial MC has been experiencing extreme rainfall events throughout the active MJO period, disaster relief efforts may be exhausted by the succession of related high impact weather events. It is vital then for forecasts to accurately represent such events with longer lead times to allow time to prepare. The high impact weather events during July 2021 presented a particular challenge for forecast models since it required for there to be not only an accurate forecast of each individual component, but their combined interactions. The representation of interactions between the CCKWs and WIGs was variable across model configurations, with parameterised models performing as well as convection-permitting models in simulating their precipitation rates over west Borneo and the trajectory of CCKW-C. A number of factors could have influenced this: first that the parameterised convection models were better able to capture the timing of the interactions between WIGs and CCKWs since they simulate rainfall associated with these processes over a wider area. Secondly the presence of the model boundaries in convection-permitting models caused boundary errors particularly associated with the WIGs so their resultant interactions may not have been faithfully represented.

When interactions between WIGs and CCKWs were faithfully represented, CCKW-C demonstrated sustained precipitation across its trajectory and over the western MC. In these model configurations, precipitation over the western MC reduced significantly following the passage of CCKW-C compared to when the rainfall over the trajectory of CCKW-C was forecasted to be weak. This demonstrates that the rainfall associated with this CCKW played a pivotal role, producing this marked shift in atmospheric conditions associated with the termination of the MJO event over

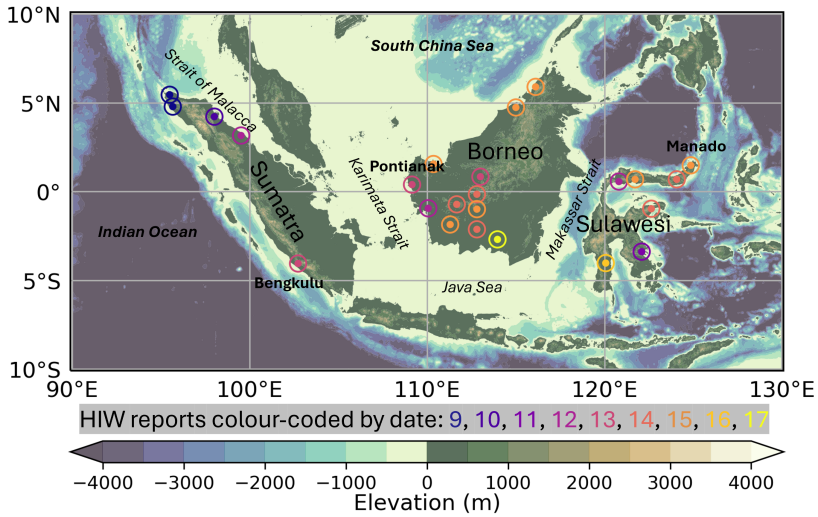


FIGURE 1 Topography of the western Maritime Continent, and locations of high impact weather events reported between 9–17 July 2021 (colour coded by date).

748 the MC.

749 acknowledgements

750 We thank Dr Adrian Lock and the two anonymous reviewers for the useful comments that improved this manuscript.
 751 This work and its contributors (NVS, AJM and BGMW) were supported by the Met Office Weather and Climate Sci-
 752 ence for Service Partnership (WCSSP) Southeast Asia as part of the Newton Fund (award P110707), and AJM was sup-
 753 ported through the TerraMaris project, funded by the Natural Environment Research Council (award NE/R016704/1).

754 data availability

755 Data used in this study are publicly available. CCKW trajectories are available through [github.com/adrianjmatthews/](https://github.com/adrianjmatthews/CCKW_database)
 756 [CCKW_database](https://github.com/adrianjmatthews/CCKW_database). The IMERG precipitation data were supplied by the National Aeronautics and Space Administration
 757 through their website at gpm.nasa.gov. ERA5 data were accessed from Copernicus at cds.climate.copernicus.eu
 758 (doi: 10.24381/cds/bd0915c6). Disaster event reports were supplied by ADInet and are available through their web-
 759 site at adinet.ahacentre.org. MetUM forecast data were supplied by Met Office, UK and are available at [zenodo.org/](https://zenodo.org/records/12760373)
 760 [records/12760373](https://zenodo.org/records/12760373) (doi: 10.5281/zenodo.12760372).

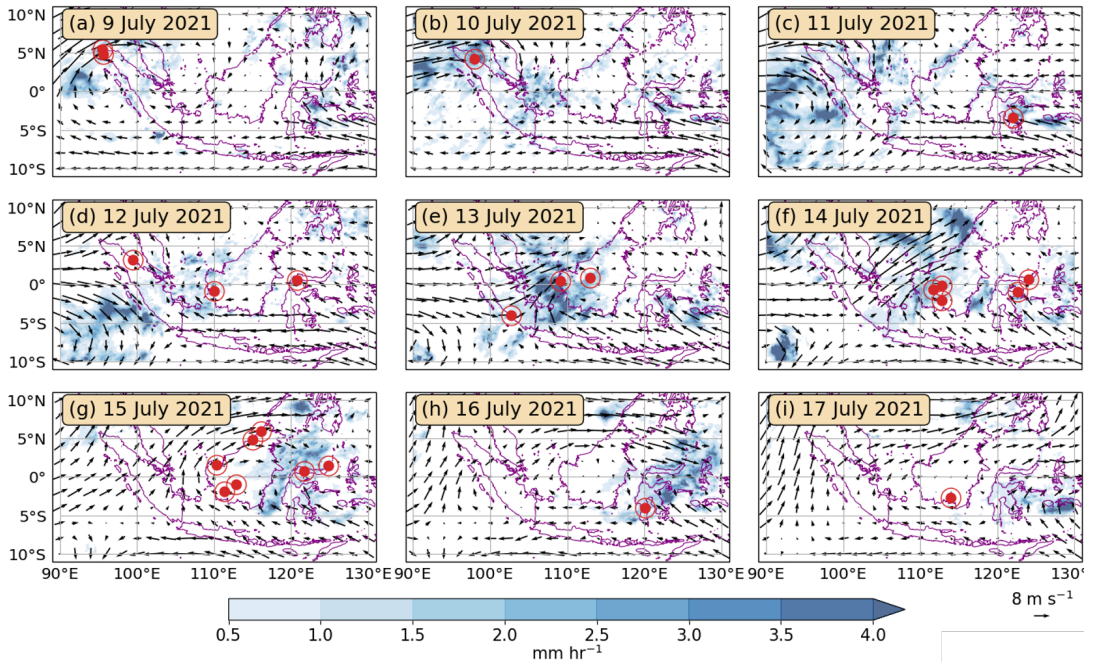


FIGURE 2 Daily average IMERG precipitation rate and ERA5 850 hPa wind vectors from 9–17 July 2021. The red markers show the locations of the HIW events identified in Figure 1.

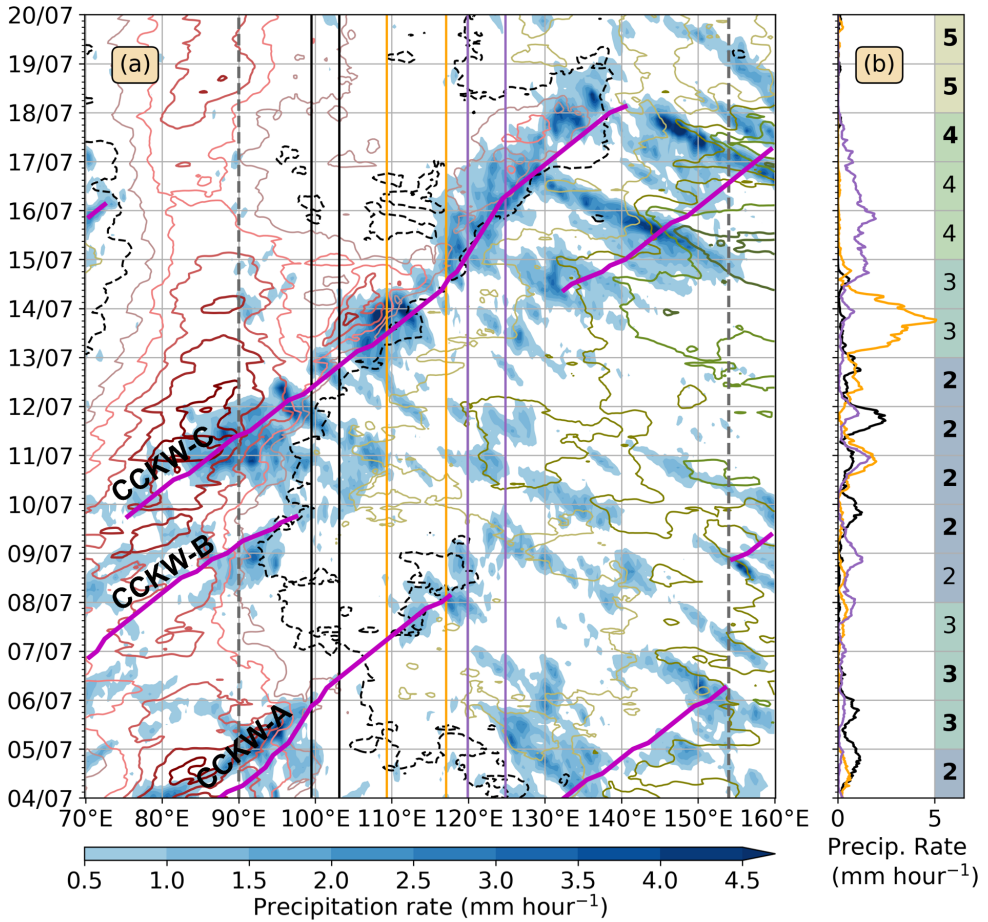


FIGURE 3 (a) Hovmöller diagram of equatorial mean (5°S–5°N) IMERG precipitation (blue colour shading) and ERA5 850 hPa zonal wind (line contours) during 4–20 July 2021. The major tick marks on the time axis correspond to 00:00 UTC. The zonal wind contour interval is 3 m s⁻¹; the zero contour is the black dashed line, positive contours are shades of red, and negative contours are shades of green. The magenta lines mark the observed CCKW trajectories. The vertical lines mark the approximate positions of the main islands (black for Sumatra, orange for Borneo, and lilac for Sulawesi). (b) Average IMERG precipitation rates (2°×2° box) centered on the west coasts of Sumatra (black), Borneo (orange) and Sulawesi (lilac). The MJO phase is given in the coloured panels in (b); the colours indicate if the MJO is active (blue, green) or suppressed (yellow) over the western MC. Normal font represents MJO amplitudes between 0.8 to 1, and bold font represents MJO amplitudes ≥ 1

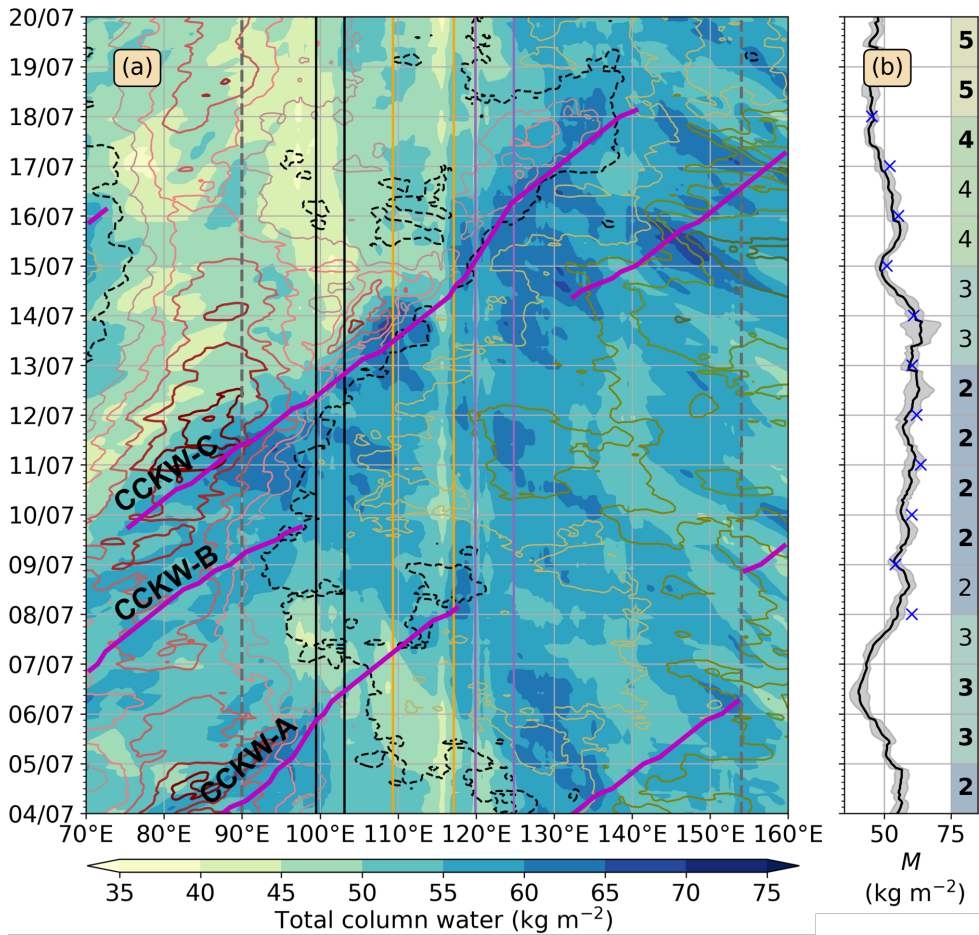


FIGURE 4 (a) Homöller diagram of equatorial mean (5°S–5°N) ERA5 total column water (M ; colour shading) and ERA5 850 hPa zonal wind (line contours) during 4–20 July 2021. The major tick marks on the time axis correspond to 00:00 UTC. The zonal wind contour interval is 3 m s^{-1} ; the zero contour is the black dashed line, positive contours are shades of red, and negative contours are shades of green. The magenta lines mark the observed CCKW trajectories. The vertical lines mark the approximate positions of the main islands (black for Sumatra, orange for Borneo, and lilac for Sulawesi). (b) Average ERA5 M ($2^\circ \times 2^\circ$ box) centered on west coast of Borneo (black line), \pm the standard deviation of grid points in the $2^\circ \times 2^\circ$ box (gray shading) and M as measured by a daily radiosonde ascent at 00:00 UTC (blue crosses). The MJO phase is given in the coloured panels in (b) (conventions are as in Figure 3).

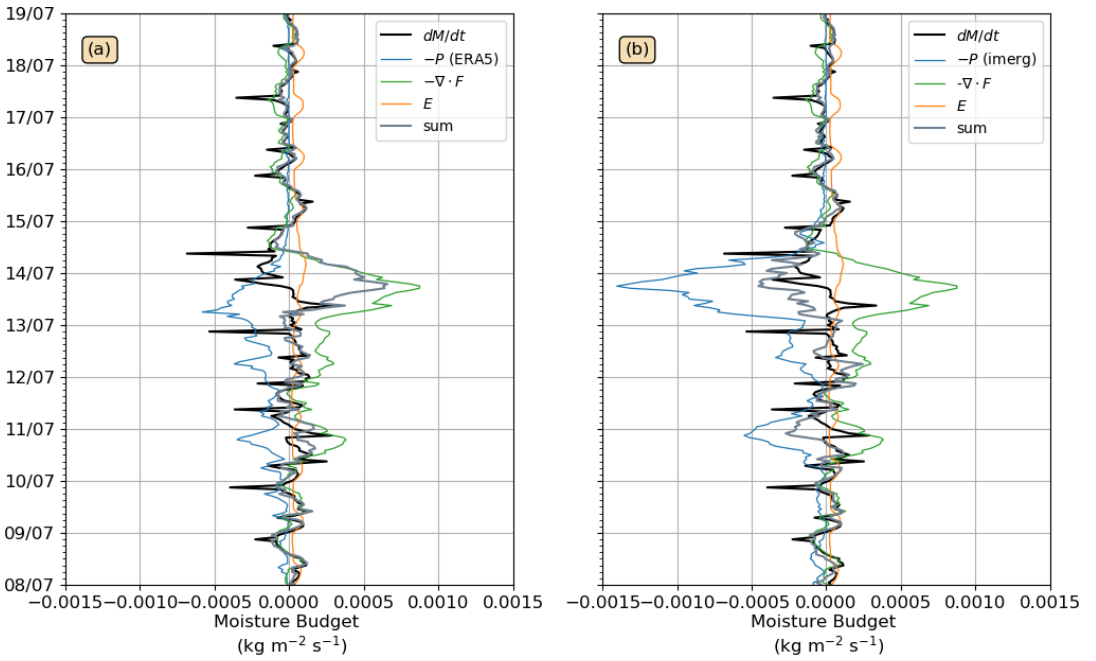


FIGURE 5 The rate of change of ERA5 total column water dM/dt averaged over the $6^\circ \times 6^\circ$ box over Pontianak (west Coast Borneo) given by (1) and source terms: ERA5 M , $\nabla \cdot F$, E and (a) ERA5 P and (b) IMERG P

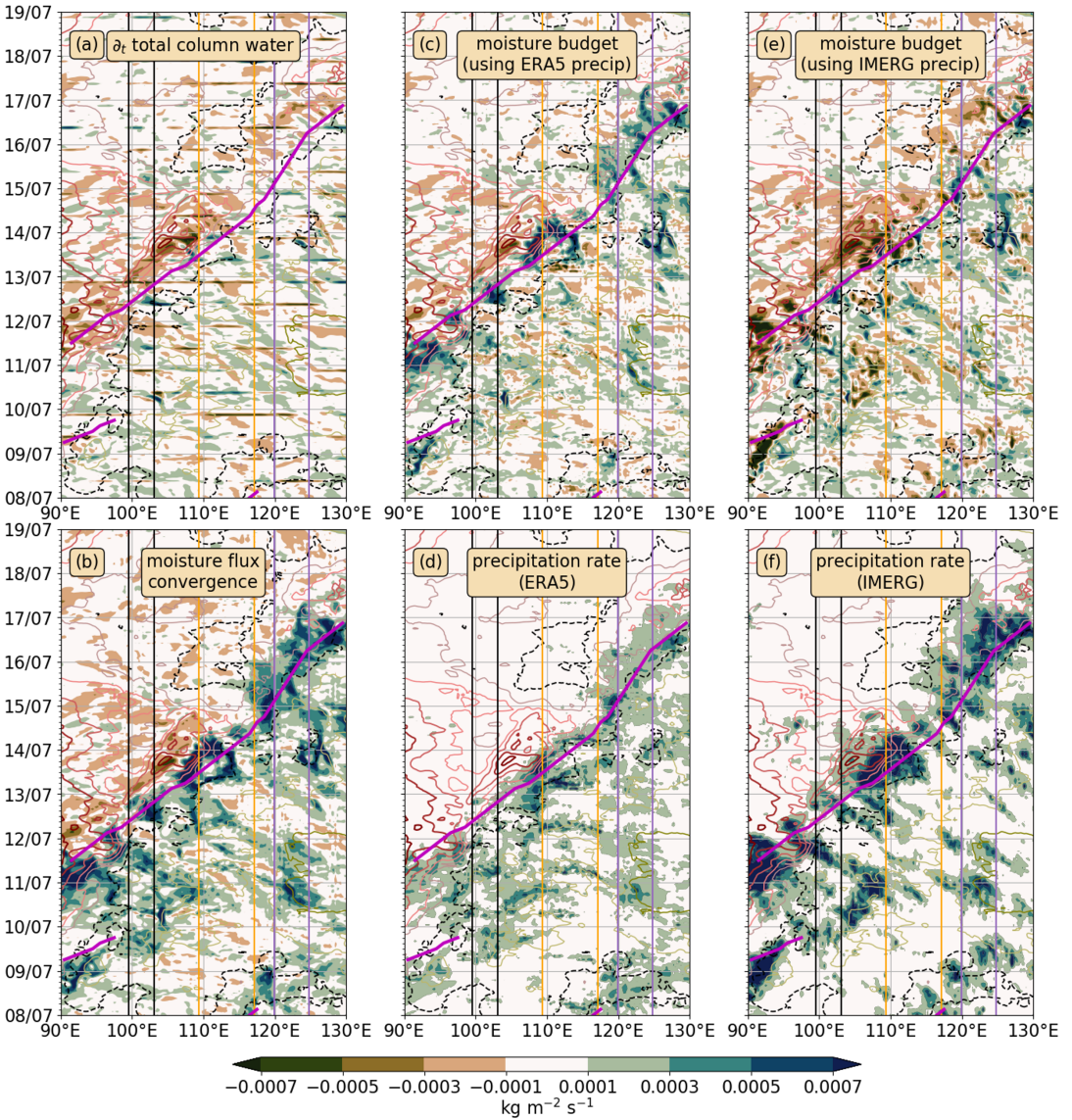


FIGURE 6 Hovmöller diagrams of (a) the time derivative of the vertically integrated total column water (b) the vertically integrated moisture flux convergence ($-\nabla \cdot \mathbf{F}$) (c) the sum of source terms using ERA5 precipitation rate (d) precipitation rate from ERA5 (e) the moisture budget estimated using IMERG precipitation rate (f) precipitation rate from IMERG. These are given for the period 8–19 July 2021 with time in UTC and averaged 3°S–3°N. ERA5 850 hPa zonal wind contours are drawn (interval 3 m s^{-1}). The first positive zonal wind shade (red) is at 3 m s^{-1} and first negative contour (green) at -3 m s^{-1} , with 0 m s^{-1} marked with a black dotted contour. The magenta line marks the observed CCKW trajectories. The vertical lines mark the approximate positions of the main islands (black for Sumatra, orange for Borneo, and lilac for Sulawesi)

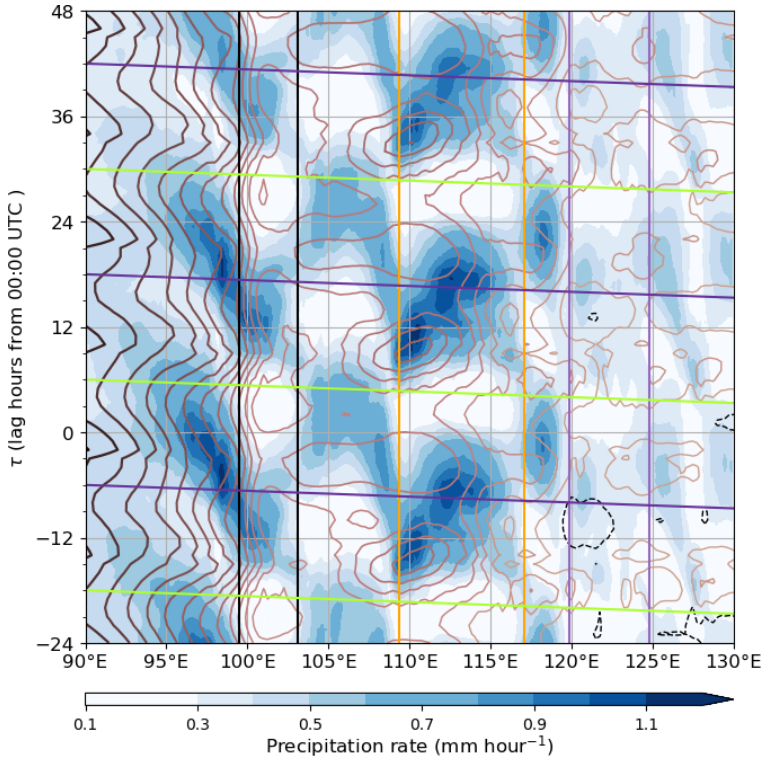


FIGURE 7 Lagged composite of the diurnal cycle of (IMERG) precipitation, defined as days where the average precipitation exceeds the 60th percentile over the western MC. The diurnal cycle of precipitation over the equatorial MC. This is calculated as lagged composites of IMERG precipitation rate (averaged between 1.5°S–1.5°N) between 2001–2022 for all days in the period where the average precipitation rate over the western equatorial MC (5°S–5°N, 95°–130°E) has exceeded the 60th percentile (0.34 mm hr⁻¹, calculated from all days between 2001–2022). The ERA5 850 hPa zonal wind is line contoured; the zero contour shown by the black dotted line, westerly winds (interval 0.4 m s⁻¹) are shown by increasingly darker and thicker brown contours. Local midday and local midnight are indicated by the green-yellow and purple horizontal lines. The vertical lines mark the approximate positions of the main islands (black for Sumatra, orange for Borneo, and lilac for Sulawesi)

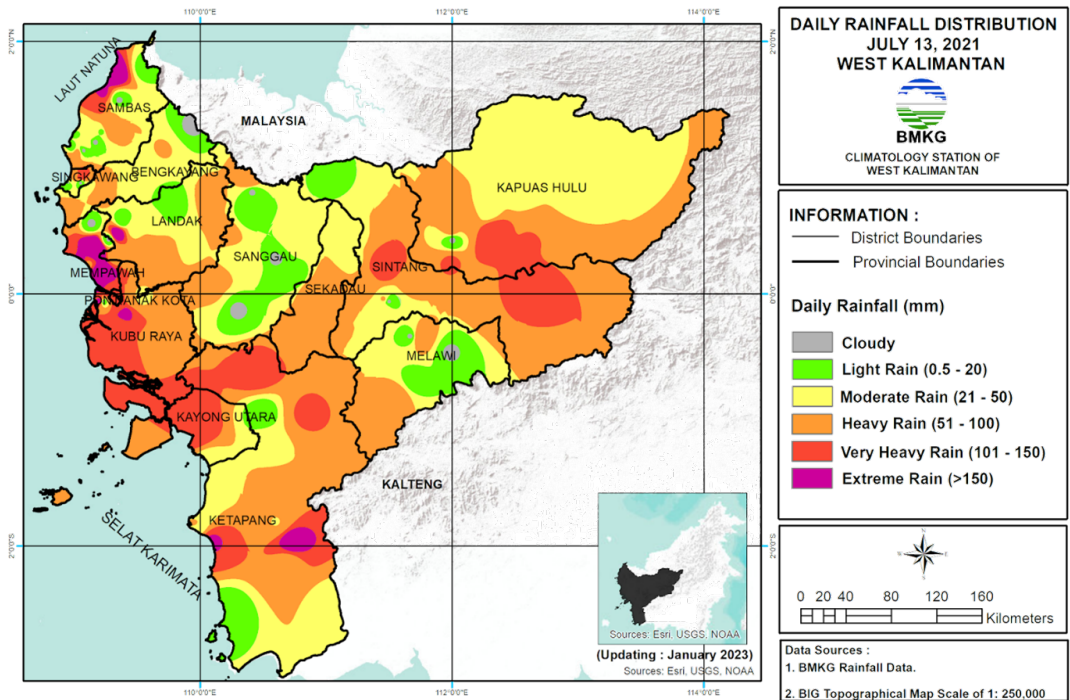


FIGURE 8 Accumulated rainfall over 13 July 2021 (beginning 00:00 UTC) as recorded by rain gauge stations in the West Kalimantan province.

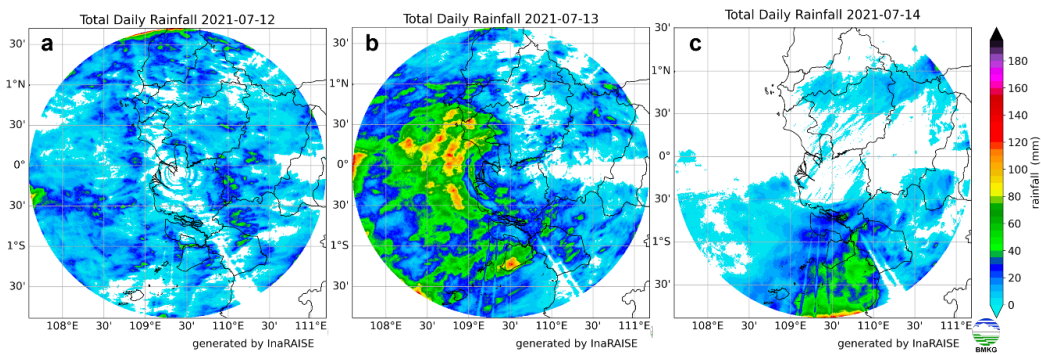


FIGURE 9 Rainfall over West Kalimantan captured by C-band Doppler radar on (a) 12 July 2021 (b) 13 July 2021 and (c) 14 July 2021. With the day beginning at 00:00 UTC. Images are generated using the InaRAISE system (Permana et al., 2019).

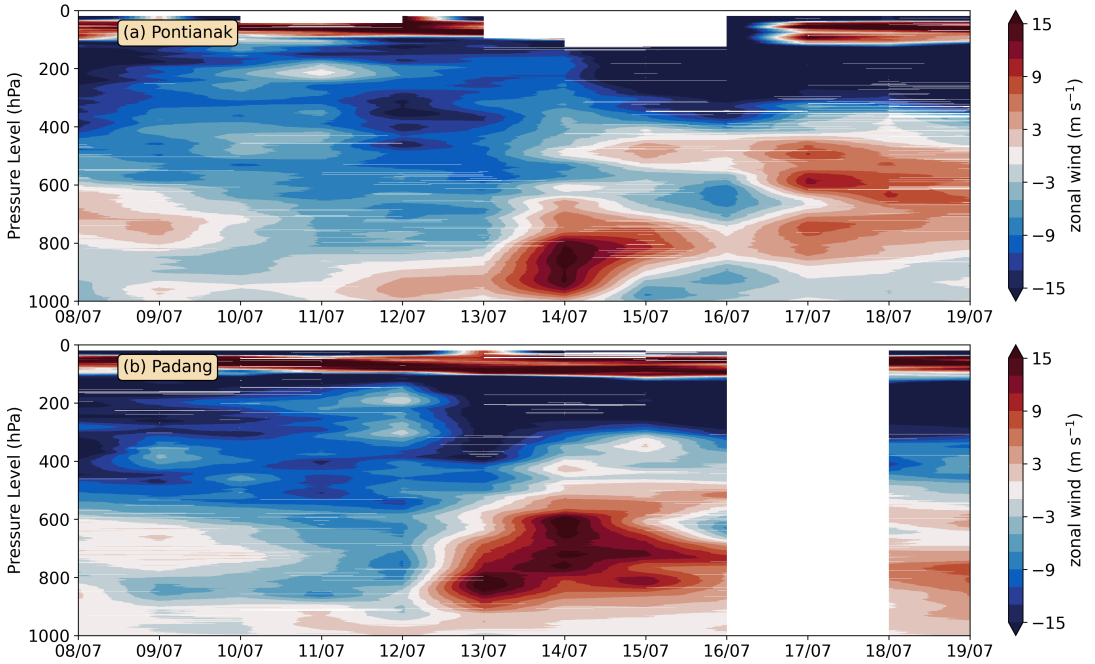


FIGURE 10 Zonal wind measured by radiosonde ascents at (a) Pontianak (west coast of Borneo) and (b) Padang (west coast of Sumatra). Ascents occurred daily at 00:00 UTC.

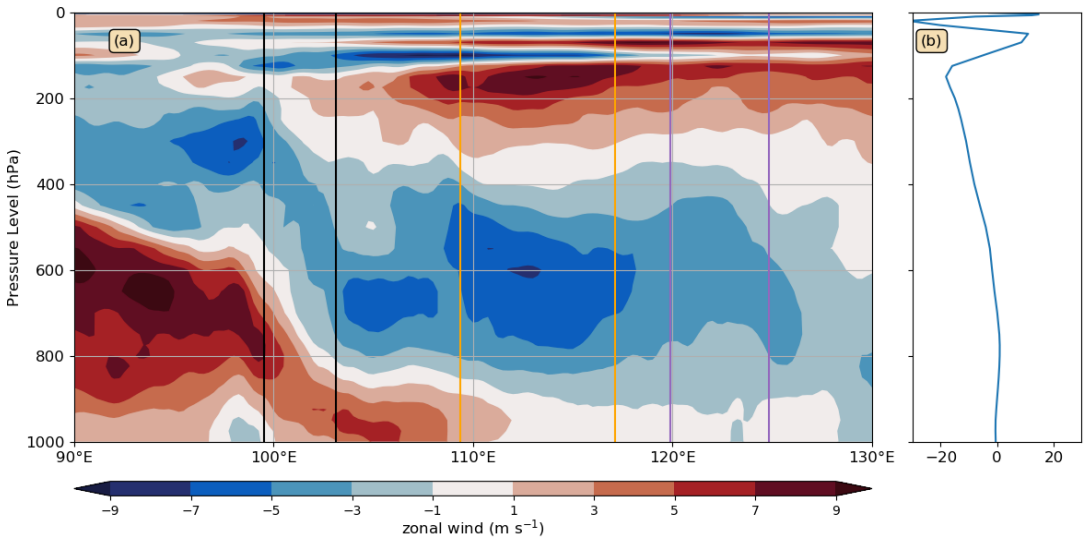


FIGURE 11 (a) ERA5 longitude-height section of zonal wind anomalies on 13 Jul 2021 at 00:00 UTC. Latitude averaged 2.5° S– 2.5° N. The anomalies are calculated with respect to (b) the longitude averaged zonal wind profile.

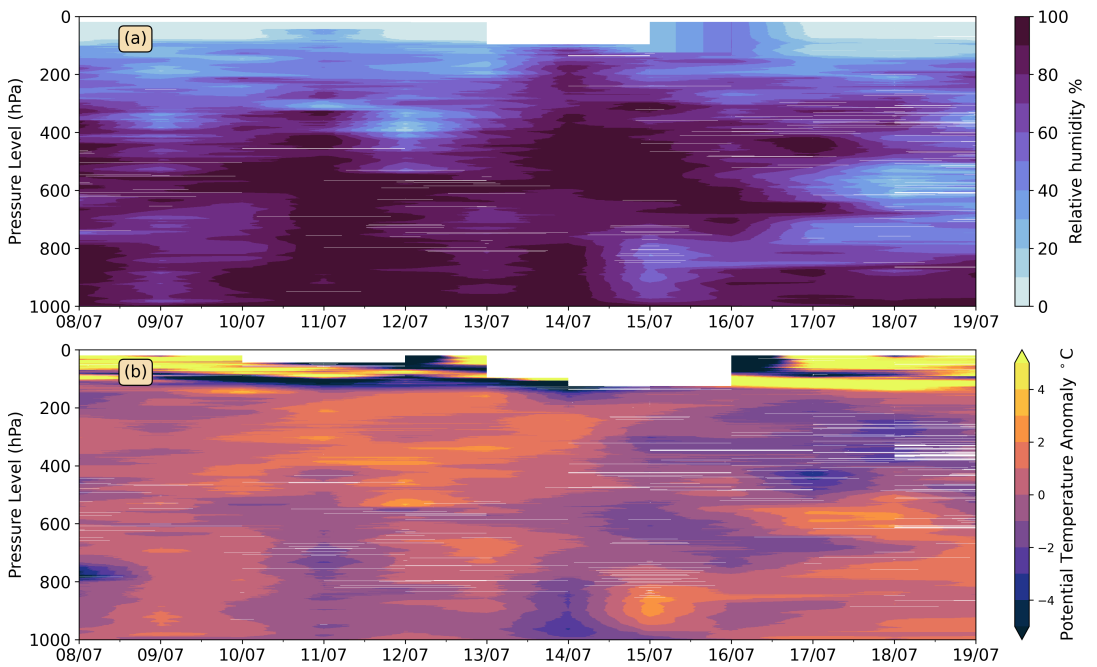


FIGURE 12 (a) Relative humidity and (b) potential temperature as measured by radiosonde ascents at Pontianak (west coast of Borneo). Ascents occurred daily at 00:00 UTC

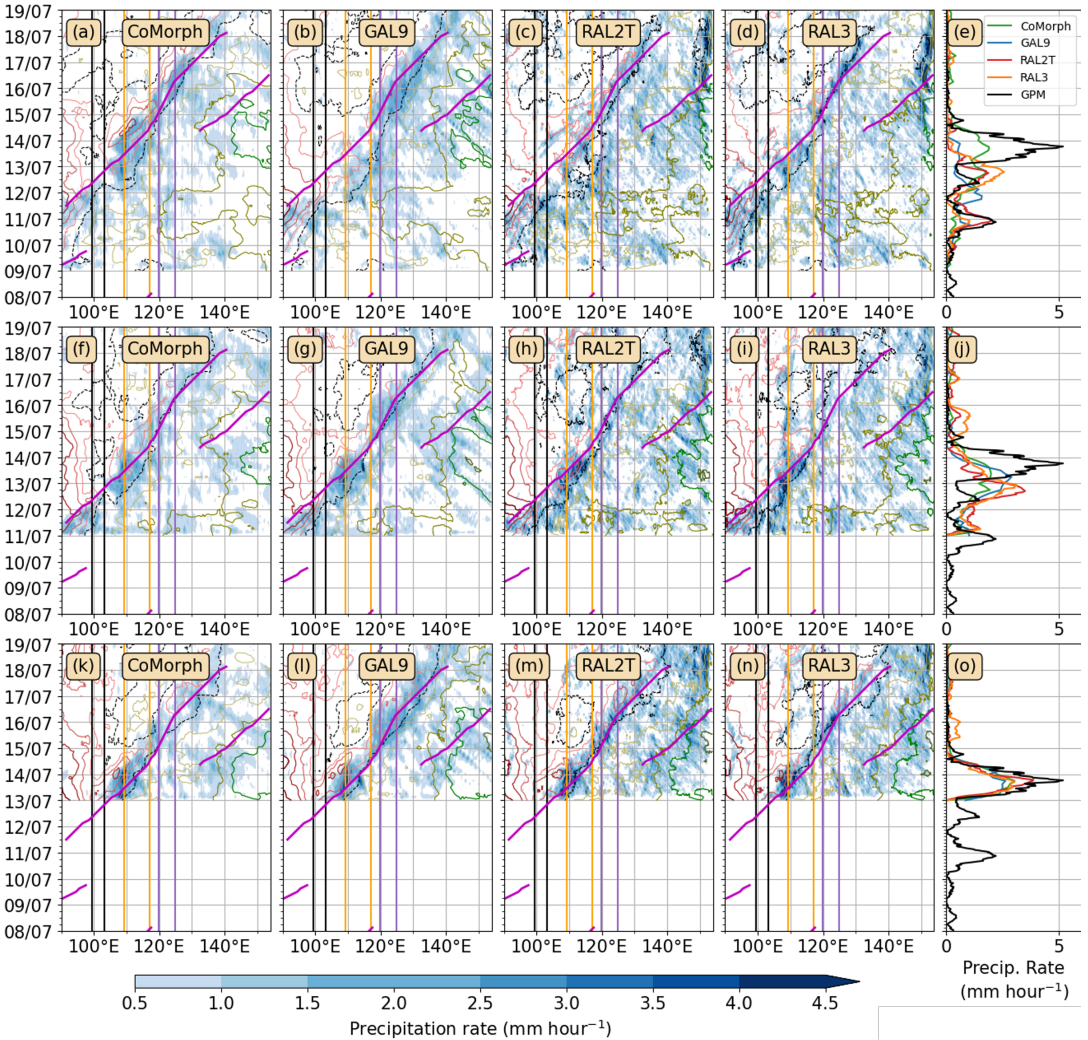


FIGURE 13 Hovmöller diagrams of deterministic MetUM forecast models averaged between 5°S - 5°N . These are organised by forecast initialisation times at 00:00 UTC: 9 July 2021 (a, b, c, d), 11 July 2021 (f, g, h, i) and 13 July 2021 (k, l, m, n) and, model configuration CoMorph A (first column), GAL9 (second column), RAL2T (third column) and RAL3 (fourth column). The average precipitation rates for each model configuration and forecast initiation time over a $6^{\circ}\text{S}\times 6^{\circ}\text{N}$ box centred on the longitude of Pontianak (west Borneo) are also given along with that of the observed IMERG precipitation rate (fifth column; e, j, o). The major tick marks on the time axis correspond to 00:00 UTC. The zonal wind contour interval is 3 m s^{-1} ; the zero contour is the black dashed line, positive contours are shades of red, and negative contours are shades of green. The magenta line marks the observed CCKW trajectories. The vertical lines mark the approximate positions of the main islands (black for Sumatra, orange for Borneo, and lilac for Sulawesi). All model results are presented on their native grids; however, Hovmöller diagrams are averaged over a wide latitude band (5°S - 5°N) and the line plots over a wide area ($6^{\circ}\text{S}\times 6^{\circ}\text{N}$) to allow for faithful comparison between model configurations.

761 **references**

- 762 S. Abhik, H. H. Hendon, and C. Zhang. The Indo-Pacific Maritime Continent Barrier Effect on MJO Prediction. Journal of
763 Climate, 36(3):945 – 957, 2023. doi: 10.1175/JCLI-D-22-0010.1. URL [clim/36/3/JCLI-D-22-0010.1.xml](https://journals.ametsoc.org/view/journals/
764 <a href=).
- 765 D. Argüeso, R. Romero, and V. Homar. Precipitation Features of the Maritime Continent in Parameterized and Explicit Con-
766 vention Models. Journal of Climate, 33(6):2449–2466, 2020. doi: 10.1175/JCLI-D-19-0416.1. URL [ametsoc.org/view/journals/clim/33/6/jcli-d-19-0416.1.xml](https://journals.
767 <a href=).
- 768 H. Bai, G. Deranadyan, C. Schumacher, A. Funk, C. Epifanio, A. Ali, Enderwin, F. Radjab, R. Adriyanto, N. Nurhayati, Y. Nugraha,
769 and A. Fauziah. Formation of Nocturnal Offshore Rainfall near the West Coast of Sumatra: Land Breeze or Gravity Wave?
770 Monthly Weather Review, 149(3):715 – 731, 2021. doi: 10.1175/MWR-D-20-0179.1. URL [org/view/journals/mwre/149/3/MWR-D-20-0179.1.xml](https://journals.ametsoc.
771 <a href=).
- 772 D. B. Baranowski, M. K. Flatau, P. J. Flatau, and A. J. Matthews. Phase locking between atmospheric convectively coupled
773 equatorial Kelvin waves and the diurnal cycle of precipitation over the Maritime Continent. Geophysical Research Letters,
774 43(15):8269–8276, 2016. doi: <https://doi.org/10.1002/2016GL069602>. URL [com/doi/abs/10.1002/2016GL069602](https://agupubs.onlinelibrary.wiley.
775 <a href=).
- 776 D. B. Baranowski, M. K. Flatau, P. J. Flatau, D. Karnawati, K. Barabasz, M. Labuz, B. Latos, J. M. Schmidt, J. A. I. Paski, and
777 Marzuki. Social-media and newspaper reports reveal large-scale meteorological drivers of floods on Sumatra. Nature
778 Communications, 11:2503, 2020. doi: 10.1038/s41467-020-16171-2. URL [https://doi.org/10.1038/s41467-020-16171-](https://doi.org/10.1038/s41467-020-16171-2)
779 [2](https://doi.org/10.1038/s41467-020-16171-2).
- 780 C. E. Birch, M. J. Roberts, L. Garcia-Carreras, D. Ackerley, M. J. Reeder, A. P. Lock, and R. Schiemann. Sea-Breeze Dynamics
781 and Convection Initiation: The Influence of Convective Parameterization in Weather and Climate Model Biases. Journal
782 of Climate, 28(20):8093 – 8108, 2015. doi: 10.1175/JCLI-D-14-00850.1. URL [journals/clim/28/20/jcli-d-14-00850.1.xml](https://journals.ametsoc.org/view/
783 <a href=).
- 784 M. Bush, I. Boutle, J. Edwards, A. Finnenkoetter, C. Franklin, K. Hanley, A. Jayakumar, H. Lewis, A. Lock, M. Mittermaier,
785 S. Mohandas, R. North, A. Porson, B. Roux, S. Webster, and M. Weeks. The second Met Office Unified Model–JULES
786 Regional Atmosphere and Land configuration, RAL2. Geoscientific Model Development, 16(6):1713–1734, 2023. doi:
787 [10.5194/gmd-16-1713-2023](https://doi.org/10.5194/gmd-16-1713-2023). URL <https://gmd.copernicus.org/articles/16/1713/2023/>.
- 788 J. Crook, F. Morris, R. G. J. Fitzpatrick, S. C. Peatman, J. Schwendike, T. H. Stein, C. E. Birch, S. Hardy, and G-Y. Yang. Impact
789 of the Madden–Julian oscillation and equatorial waves on tracked mesoscale convective systems over southeast Asia.
790 Quarterly Journal of the Royal Meteorological Society, 150(760):1724–1751, 2024. doi: <https://doi.org/10.1002/qj.4667>.
791 URL <https://rmets.onlinelibrary.wiley.com/doi/abs/10.1002/qj.4667>.
- 792 N. A. Da Silva and A. J. Matthews. Impact of the Madden–Julian Oscillation on extreme precipitation over the western
793 Maritime Continent and Southeast Asia. Quarterly Journal of the Royal Meteorological Society, 147(739):3434–3453,
794 2021. doi: <https://doi.org/10.1002/qj.4136>. URL <https://rmets.onlinelibrary.wiley.com/doi/abs/10.1002/qj.4136>.
- 795 J. Dias, M. Gehne, G. N. Kiladis, N. Sakaeda, P. Bechtold, and T. Haiden. Equatorial Waves and the Skill of NCEP and ECMWF
796 Numerical Weather Prediction Systems. Monthly Weather Review, 146(6):1763–1784, 2018. doi: 10.1175/MWR-D-17-
797 0362.1. URL <https://journals.ametsoc.org/view/journals/clim/33/8/jcli-d-19-0043.1.xml>.
- 798 Z. Feng, L. R. Leung, J. Hardin, C. R. Terai, F. Song, and P. Caldwell. Mesoscale Convective Systems in DYAMOND
799 Global Convection-Permitting Simulations. Geophysical Research Letters, 50(4):e2022GL102603, 2023. doi: <https://doi.org/10.1029/2022GL102603>. URL <https://agupubs.onlinelibrary.wiley.com/doi/abs/10.1029/2022GL102603>.
800 [e2022GL102603](https://doi.org/10.1029/2022GL102603). URL <https://agupubs.onlinelibrary.wiley.com/doi/abs/10.1029/2022GL102603>.
801 [e2022GL102603](https://doi.org/10.1029/2022GL102603).
- 802 S. Ferrett, G-Y. Yang, S. J. Woolnough, J. Methven, K. Hodges, and C. E. Holloway. Linking extreme precipitation in Southeast
803 Asia to equatorial waves. Quarterly Journal of the Royal Meteorological Society, 146(727):665–684, 2020. doi: <https://doi.org/10.1002/qj.3699>. URL <https://rmets.onlinelibrary.wiley.com/doi/abs/10.1002/qj.3699>.
804 [//doi.org/10.1002/qj.3699](https://doi.org/10.1002/qj.3699). URL <https://rmets.onlinelibrary.wiley.com/doi/abs/10.1002/qj.3699>.

- 805 S. Ferrett, J. Methven, S. J. Woolnough, G-Y Yang, C. E. Holloway, and G. Wolf. Hybrid Dynamical–Statistical Forecasts of the
806 Risk of Rainfall in Southeast Asia Dependent on Equatorial Waves. *Monthly Weather Review*, 151(8):2139 – 2152, 2023.
807 doi: 10.1175/MWR-D-22-0300.1. URL <https://rmets.onlinelibrary.wiley.com/doi/abs/10.1002/qj.3699>.
- 808 P. R. Field, A. Hill, B. Shipway, K. Furtado, J. Wilkinson, A. Miltenberger, H. Gordon, D. P. Grosvenor, R. Stevens, and K. Van
809 Weverberg. Implementation of a double moment cloud microphysics scheme in the uk met office regional numerical
810 weather prediction model. *Quarterly Journal of the Royal Meteorological Society*, 149(752):703–739, 2023. doi: <https://doi.org/10.1002/qj.4414>. URL <https://rmets.onlinelibrary.wiley.com/doi/abs/10.1002/qj.4414>.
- 812 O. S. Hai, A. A. Samah, S. N. Chenoli, K. Subramaniam, and M. Y. A. Mazuki. Extreme Rainstorms that Caused Devastating
813 Flooding across the East Coast of Peninsular Malaysia during November and December 2014. *Weather and Forecasting*,
814 32(3):849–872, 2017. doi: 10.1175/WAF-D-16-0160.1. URL https://journals.ametsoc.org/view/journals/wefo/32/3/waf-d-16-0160_1.xml.
- 816 K. Halladay, R. Kahana, B. Johnson, C. Still, G. Fosser, and L. Alves. Convection-permitting climate simulations for South
817 America with the Met Office Unified Model. *Climate Dynamics*, 61(11):5247–5269, 2023. doi: 10.1007/s00382-023-
818 06853-0.
- 819 E. Hermawan, S. W. Lubis, T. Harjana, A. Purwaningsih, Risyanto, A. Ridho, D. F. Andarini, D. N. Ratri, and R. Widyarningsih.
820 Large-Scale Meteorological Drivers of the Extreme Precipitation Event and Devastating Floods of Early-February 2021
821 in Semarang, Central Java, Indonesia. *Atmosphere*, 13(7), 2022. ISSN 2073-4433. doi: 10.3390/atmos13071092. URL
822 <https://www.mdpi.com/2073-4433/13/7/1092>.
- 823 H. Hersbach, B. Bell, P. Berrisford, S. Hirahara, A. Horányi, J. Muñoz-Sabater, J. Nicolas, C. Peubey, R. Radu, D. Schepers,
824 A. Simmons, C. Soci, S. Abdalla, X. Abellan, G. Balsamo, P. Bechtold, G. Biavati, J. Bidlot, M. Bonavita, G. De Chiara,
825 P. Dahlgren, D. Dee, M. Diamantakis, R. Dragani, J. Flemming, R. Forbes, M. Fuentes, A. Geer, L. Haimberger, S. Healy, R. J.
826 Hogan, E. Hólm, M. Janisková, S. Keeley, P. Laloyaux, P. Lopez, C. Lupu, G. Radnoti, P. de Rosnay, I. Rozum, F. Vamborg,
827 S. Villaume, and J.-N. Thépaut. The ERA5 global reanalysis. *Quarterly Journal of the Royal Meteorological Society*, 146
828 (730):1999–2049, 2020. doi: <https://doi.org/10.1002/qj.3803>. URL <https://rmets.onlinelibrary.wiley.com/doi/abs/10.1002/qj.3803>.
- 830 R. Honnert, G. A. Efstathiou, R. J. Beare, J. Ito, A. Lock, R. Neggers, R. S. Plant, H. H. Shin, L. Tomassini, and B. Zhou. The atmo-
831 spheric boundary layer and the “gray zone” of turbulence: A critical review. *Journal of Geophysical Research: Atmospheres*,
832 125(13):e2019JD030317, 2020. doi: <https://doi.org/10.1029/2019JD030317>. URL <https://agupubs.onlinelibrary.wiley.com/doi/abs/10.1029/2019JD030317>.
- 834 G. J. Huffman, D. T. Bolvin, E. J. Nelkin, and J. Tan. Integrated Multi-satellitE Retrievals for GPM (IMERG) technical documen-
835 tation. Technical report, 2020. URL https://docsserver.gesdisc.eosdis.nasa.gov/public/project/GPM/IMERG_doc.06.pdf.
- 837 P. M. Inness and J. M. Slingo. The interaction of the Madden–Julian Oscillation with the Maritime Continent in a GCM.
838 *Quarterly Journal of the Royal Meteorological Society*, 132(618):1645–1667, 2006. doi: <https://doi.org/10.1256/qj.05.102>.
839 URL <https://rmets.onlinelibrary.wiley.com/doi/abs/10.1256/qj.05.102>.
- 840 G. N. Kiladis, M. C. Wheeler, P. T. Haertel, K. H. Straub, and P. E. Roundy. Convectively coupled equatorial waves. *Reviews*
841 *of Geophysics*, 47(2), 2009. doi: <https://doi.org/10.1029/2008RG000266>. URL <https://agupubs.onlinelibrary.wiley.com/doi/abs/10.1029/2008RG000266>.
- 843 H-M Kim, D. Kim, F. Vitart, V. E. Toma, J-S Kug, and P. J. Webster. MJO Propagation across the Maritime Continent in the
844 ECMWF Ensemble Prediction System. *Journal of Climate*, 29(11):3973 – 3988, 2016. doi: 10.1175/JCLI-D-15-0862.1.
845 URL <https://journals.ametsoc.org/view/journals/clim/29/11/jcli-d-15-0862.1.xml>.
- 846 B. Latos, T. Lefort, M. K. Flatau, P. J. Flatau, D. S. Permana, D. B. Baranowski, J. A. I. Paski, E. Makmur, E. Sulystyo, P. Peyrillé,
847 Z. Feng, A. J. Matthews, and J. M. Schmidt. Equatorial Waves Triggering Extreme Rainfall and Floods in Southwest Sulawesi,
848 Indonesia. *Monthly Weather Review*, 149(5):1381 – 1401, 2021. doi: 10.1175/MWR-D-20-0262.1. URL <https://journals.ametsoc.org/view/journals/mwre/149/5/MWR-D-20-0262.1.xml>.
- 849

- 850 S. L. Lavender, A. J. Stirling, M. Whittall, R. A. Stratton, C. L. Daleu, R. S. Plant, A. Lock, and J-F. Gu. The use of ide-
851 alised experiments in testing a new convective parametrization: Performance of CoMorph-A. Quarterly Journal of
852 the Royal Meteorological Society, 150(760):1581–1600, 2024. doi: <https://doi.org/10.1002/qj.4660>. URL [https://](https://rmets.onlinelibrary.wiley.com/doi/abs/10.1002/qj.4660)
853 rmets.onlinelibrary.wiley.com/doi/abs/10.1002/qj.4660.
- 854 B. Liebmann, H. H. Hendon, and J. D. Glick. On the Generation of Two-Day Convective Disturbances Across the Western
855 Equatorial Pacific. Journal of the Meteorological Society of Japan. Ser. II, 75(4):939–946, 1997. doi: 10.2151/jmsj1965.
856 75.4_939.
- 857 A. P. Lock, M. Whittall, A. J. Stirling, K. D. Williams, S.L. Lavender, C. Morcrette, K. Matsubayashi, P.R. Field, G. Martin, M. Willett,
858 and J. Heming. The performance of the comorph-a convection package in global simulations with the met office unified
859 model. Quarterly Journal of the Royal Meteorological Society (accepted), 2024.
- 860 B. S. Love, A. J. Matthews, and G. M. S. Lister. The diurnal cycle of precipitation over the Maritime Continent in a high-
861 resolution atmospheric model. Quarterly Journal of the Royal Meteorological Society, 137(657):934–947, 2011. doi:
862 <https://doi.org/10.1002/qj.809>. URL [https://](https://rmets.onlinelibrary.wiley.com/doi/abs/10.1002/qj.809)
rmets.onlinelibrary.wiley.com/doi/abs/10.1002/qj.809.
- 863 S. W. Lubis and M. R. Respati. Impacts of convectively coupled equatorial waves on rainfall extremes in Java, Indonesia.
864 International Journal of Climatology, 41(4):2418–2440, 2021. doi: <https://doi.org/10.1002/joc.6967>. URL [https://](https://rmets.onlinelibrary.wiley.com/doi/abs/10.1002/joc.6967)
865 rmets.onlinelibrary.wiley.com/doi/abs/10.1002/joc.6967.
- 866 S. W. Lubis, S. Hagos, E. Hermawan, M. R. Respati, A. Ridho, Risyanto, J. A. I. Paski, F. R. Muhammad, Siswanto, D. N. Ratri,
867 S. Setiawan, and D. S. Permana. Record-Breaking Precipitation in Indonesia’s Capital of Jakarta in Early January 2020
868 Linked to the Northerly Surge, Equatorial Waves, and MJO. Geophysical Research Letters, 49(22):e2022GL101513,
869 2022. doi: <https://doi.org/10.1029/2022GL101513>. URL [https://](https://agupubs.onlinelibrary.wiley.com/doi/abs/10.1029/2022GL101513)
870 agupubs.onlinelibrary.wiley.com/doi/abs/10.1029/2022GL101513. e2022GL101513 2022GL101513.
- 871 R. A. Madden and P. R. Julian. Description of Global-Scale Circulation Cells in the Tropics with a 40–50 Day Period. Journal
872 of Atmospheric Sciences, 29(6):1109 – 1123, 1972. doi: 10.1175/1520-0469(1972)029<1109:DOGSCC>2.0.CO;2. URL
873 https://journals.ametsoc.org/view/journals/atsc/29/6/1520-0469_1972_029_1109_dogsc_2_0_co_2.xml.
- 874 A. J. Matthews. Dynamical propagation and growth mechanisms for convectively coupled equatorial Kelvin waves over the
875 Indian Ocean. Quarterly Journal of the Royal Meteorological Society, 147(741):4310–4336, 2021. doi: [https://doi.org/](https://doi.org/10.1002/qj.4179)
876 [10.1002/qj.4179](https://doi.org/10.1002/qj.4179). URL <https://rmets.onlinelibrary.wiley.com/doi/abs/10.1002/qj.4179>.
- 877 M. B. Menary, T. Kuhlbrodt, J. Ridley, M. B. Andrews, O. B. Dimdore-Miles, J. Deshayes, R. Eade, L. Gray, S. Ineson, J. Mignot,
878 C. D. Roberts, J. Robson, R. A. Wood, and P. Xavier. Preindustrial Control Simulations With HadGEM3-GC3.1 for CMIP6.
879 Journal of Advances in Modeling Earth Systems, 10(12):3049–3075, 2018. doi: <https://doi.org/10.1029/2018MS001495>.
880 URL <https://agupubs.onlinelibrary.wiley.com/doi/abs/10.1029/2018MS001495>.
- 881 T. Nakazawa. Tropical Super Clusters within Intraseasonal Variations over the Western Pacific. Journal of the Meteorological
882 Society of Japan. Ser. II, 66(6):823–839, 1988. doi: 10.2151/jmsj1965.66.6_823.
- 883 S. C. Peatman, A. J. Matthews, and D. P. Stevens. Propagation of the Madden–Julian Oscillation through the Maritime Conti-
884 nent and scale interaction with the diurnal cycle of precipitation. Quarterly Journal of the Royal Meteorological Society,
885 140(680):814–825, 2014. doi: 10.1002/qj.2161.
- 886 S. C. Peatman, J. Schwendike, C. E. Birch, J. H. Marsham, A. J. Matthews, and G.-Y. Yang. A Local-to-Large Scale View of
887 Maritime Continent Rainfall: Control by ENSO, MJO, and Equatorial Waves. Journal of Climate, 34(22):8933 – 8953,
888 2021. doi: 10.1175/JCLI-D-21-0263.1. URL [https://journals.ametsoc.org/view/journals/clim/34/22/JCLI-D-21-](https://journals.ametsoc.org/view/journals/clim/34/22/JCLI-D-21-0263.1.xml)
889 [0263.1.xml](https://journals.ametsoc.org/view/journals/clim/34/22/JCLI-D-21-0263.1.xml).
- 890 S. C. Peatman, C. E. Birch, J. Schwendike, J. H. Marsham, C. Dearden, S. Webster, R. R. Neely, and A. J. Matthews. The Role of
891 Density Currents and Gravity Waves in the Offshore Propagation of Convection over Sumatra. Monthly Weather Review,
892 151(7):1757 – 1777, 2023. doi: 10.1175/MWR-D-22-0322.1. URL [https://journals.ametsoc.org/view/journals/mwre/](https://journals.ametsoc.org/view/journals/mwre/151/7/MWR-D-22-0322.1.xml)
893 [151/7/MWR-D-22-0322.1.xml](https://journals.ametsoc.org/view/journals/mwre/151/7/MWR-D-22-0322.1.xml).

- 894 D. S. Permana, T. D. Hutapea, A. S. Praja, J. A. I. Paski, E. E. S. Makmur, U. Haryoko, I. H. Umam, M. Saepudin, and R. Adriyanto.
895 The Indonesia In-House Radar Integration System (InaRAISE) of Indonesian Agency for Meteorology Climatology and
896 Geophysics (BMKG): Development, Constraint, and Progress. IOP Conference Series: Earth and Environmental Science,
897 303(1):012051, 2019. doi: 10.1088/1755-1315/303/1/012051.
- 898 A. F. Prein, W. Langhans, G. Fosser, A. Ferrone, N. Ban, K. Goergen, M. Keller, M. Tölle, O. Gutjahr, F. Feser, E. Brisson,
899 S. Kollet, J. Schmidli, N. P. M. van Lipzig, and R. Leung. A review on regional convection-permitting climate modeling:
900 Demonstrations, prospects, and challenges. Reviews of Geophysics, 53(2):323–361, 2015. doi: [https://doi.org/10.1002/](https://doi.org/10.1002/2014RG000475)
901 [2014RG000475](https://doi.org/10.1002/2014RG000475). URL <https://agupubs.onlinelibrary.wiley.com/doi/abs/10.1002/2014RG000475>.
- 902 A. Purwaningsih, S. W. Lubis, E. Hermawan, D. F. Andarini, T. Harjana, D. N. Ratri, A. Ridho, Risyanto, and A. P. Sujalu. Moisture
903 Origin and Transport for Extreme Precipitation over Indonesia's New Capital City, Nusantara in August 2021. Atmosphere,
904 13(9), 2022. ISSN 2073-4433. doi: 10.3390/atmos13091391. URL <https://www.mdpi.com/2073-4433/13/9/1391>.
- 905 J.-H. Qian. Why Precipitation Is Mostly Concentrated over Islands in the Maritime Continent. Journal of the Atmospheric
906 Sciences, 65(4):1428 – 1441, 2008. doi: 10.1175/2007JAS2422.1. URL [https://journals.ametsoc.org/view/journals/](https://journals.ametsoc.org/view/journals/atasc/65/4/2007jas2422.1.xml)
907 [atasc/65/4/2007jas2422.1.xml](https://journals.ametsoc.org/view/journals/atasc/65/4/2007jas2422.1.xml).
- 908 C. S. Ramage. Role of a tropical "Maritime Continent" in the atmospheric circulation. Monthly Weather Review, 96(6):365 –
909 370, 1968. doi: 10.1175/1520-0493(1968)096<0365:ROATMC>2.0.CO;2. URL [https://journals.ametsoc.org/view/](https://journals.ametsoc.org/view/journals/mwre/96/6/1520-0493_1968_096_0365_roatmc_2_0_co_2.xml)
910 [journals/mwre/96/6/1520-0493_1968_096_0365_roatmc_2_0_co_2.xml](https://journals.ametsoc.org/view/journals/mwre/96/6/1520-0493_1968_096_0365_roatmc_2_0_co_2.xml).
- 911 M. J. Roberts, A. Baker, E. W. Blockley, D. Calvert, A. Coward, H. T. Hewitt, L. C. Jackson, T. Kuhlbrodt, P. Mathiot, C. D.
912 Roberts, R. Schiemann, J. Seddon, B. Vannière, and P. L. Vidale. Description of the resolution hierarchy of the global
913 coupled HadGEM3-GC3.1 model as used in CMIP6 HighResMIP experiments. Geoscientific Model Development, 12(12):
914 4999–5028, 2019. doi: 10.5194/gmd-12-4999-2019. URL <https://gmd.copernicus.org/articles/12/4999/2019/>.
- 915 D. P. Rowell, E. J. Kendon, M. J. Roberts, R. A. Stratton, J. A. Crook, and C. Wilcox. Improved climatological precipitation
916 characteristics over West Africa at convection-permitting scales. Climate Dynamics, 53(3):1991–2011, 2019. doi: 10.
917 1007/s00382-019-04759-4.
- 918 J. H. Ruppert and F. Zhang. Diurnal Forcing and Phase Locking of Gravity Waves in the Maritime Continent. Journal of the
919 Atmospheric Sciences, 76(9):2815 – 2835, 2019. doi: 10.1175/JAS-D-19-0061.1. URL [https://journals.ametsoc.org/](https://journals.ametsoc.org/view/journals/atasc/76/9/jas-d-19-0061.1.xml)
920 [view/journals/atasc/76/9/jas-d-19-0061.1.xml](https://journals.ametsoc.org/view/journals/atasc/76/9/jas-d-19-0061.1.xml).
- 921 N. V. Senior, A. J. Matthews, B. G. M. Webber, S. Webster, R. W. Jones, D. S. Permana, J. A. I. Paski, and R. Fadila. Ex-
922 treme precipitation at Padang, Sumatra triggered by convectively coupled Kelvin waves. Quarterly Journal of the
923 Royal Meteorological Society, 149(755):2281–2300, 2023. doi: <https://doi.org/10.1002/qj.4506>. URL <https://rmetsonlineibrary.wiley.com/doi/abs/10.1002/qj.4506>.
- 924
- 925 C. J. Short and J. Petch. Reducing the spin-up of a regional NWP system without data assimilation. Quarterly Journal of the Royal Meteorological Society, 148(745):1623–1643, 2022. doi: [https://doi.org/10.1002/](https://doi.org/10.1002/qj.4268)
926 [qj.4268](https://doi.org/10.1002/qj.4268).
927
- 928 Y. N. Takayabu. Large-Scale Cloud Disturbances Associated with Equatorial Waves: Part II Westward-Propagating Inertio-
929 Gravity Waves. Journal of the Meteorological Society of Japan. Ser. II, 72(3):451–465, 1994. doi: 10.2151/jmsj1965.72.
930 3_451.
- 931 L. Tomassini, M. Willett, A. Sellar, A. Lock, D. Walters, M. Whitall, C. Sanchez, J. Heming, P. Earnshaw, J. M. Rodriguez, D.n
932 Ackerley, P. Xavier, C. Franklin, and C. A. Senior. Confronting the convective gray zone in the global configuration of the
933 met office unified model. Journal of Advances in Modeling Earth Systems, 15(5):e2022MS003418, 2023. doi: <https://doi.org/10.1029/2022MS003418>. URL <https://agupubs.onlinelibrary.wiley.com/doi/abs/10.1029/2022MS003418>.
934
- 935 K. Van Weverberg, C. J. Morcrette, I. Boutle, K. Furtado, and P. R. Field. A Bimodal Diagnostic Cloud Fraction Parameterization.
936 Part I: Motivating Analysis and Scheme Description. Monthly Weather Review, 149(3):841 – 857, 2021. doi: 10.1175/
937 MWR-D-20-0224.1. URL <https://journals.ametsoc.org/view/journals/mwre/149/3/MWR-D-20-0224.1.xml>.

- 938 C. L. Vincent and T. P. Lane. Mesoscale Variation in Diabatic Heating around Sumatra, and Its Modulation with the Mad-
939 den-Julian Oscillation. *Monthly Weather Review*, 146(8):2599–2614, 2018. doi: 10.1175/MWR-D-17-0392.1.
- 940 D. Walters, A. J. Baran, I. Boutle, M. Brooks, P. Earnshaw, J. Edwards, K. Furtado, P. Hill, A. Lock, J. Manners, C. Morcrette,
941 J. Mulcahy, C. Sanchez, C. Smith, R. Stratton, W. Tennant, L. Tomassini, K. Van Weverberg, S. Vosper, M. Willett, J. Browse,
942 A. Bushell, K. Carslaw, M. Dalvi, R. Essery, N. Gedney, S. Hardiman, B. Johnson, C. Johnson, A. Jones, C. Jones, G. Mann,
943 S. Milton, H. Rumbold, A. Sellar, M. Ujji, M. Whittall, K. Williams, and M. Zerroukat. The Met Office Unified Model Global
944 Atmosphere 7.0/7.1 and JULES Global Land 7.0 configurations. *Geoscientific Model Development*, 12(5):1909–1963,
945 2019. doi: 10.5194/gmd-12-1909-2019. URL <https://gmd.copernicus.org/articles/12/1909/2019/>.
- 946 Y. Wei, Z. Pu, and C. Zhang. Diurnal Cycle of Precipitation Over the Maritime Continent Under Modulation of MJO: Perspec-
947 tives From Cloud-Permitting Scale Simulations. *Journal of Geophysical Research: Atmospheres*, 125(13):e2020JD032529,
948 2020. doi: <https://doi.org/10.1029/2020JD032529>. URL <https://agupubs.onlinelibrary.wiley.com/doi/abs/10.1029/2020JD032529>. e2020JD032529 2020JD032529.
- 950 M. Wheeler and G. N. Kiladis. Convectively Coupled Equatorial Waves: Analysis of Clouds and Temperature in the Wavenum-
951 ber-Frequency Domain. *Journal of the Atmospheric Sciences*, 56(3):374 – 399, 1999. doi: 10.1175/1520-0469(1999)
952 056<0374:CCEWAO>2.0.CO;2. URL https://journals.ametsoc.org/view/journals/atsc/56/3/1520-0469_1999_056_0374_ccewao_2.0.co_2.xml.
- 954 M. C. Wheeler and H. H. Hendon. An All-Season Real-Time Multivariate MJO Index: Development of an Index for
955 Monitoring and Prediction. *Monthly Weather Review*, 132(8):1917 – 1932, 2004. doi: 10.1175/1520-0493(2004)
956 132<1917:AARMMI>2.0.CO;2. URL https://journals.ametsoc.org/view/journals/mwre/132/8/1520-0493_2004_132_1917_aarmmi_2.0.co_2.xml.
- 958 K. D. Williams, D. Copey, E. W. Blockley, A. Bodas-Salcedo, D. Calvert, R. Comer, P. Davis, T. Graham, H. T. Hewitt, R. Hill,
959 P. Hyder, S. Ineson, T. C. Johns, A. B. Keen, R. W. Lee, A. Megann, S. F. Milton, J. G. L. Rae, M. J. Roberts, A. A. Scaife,
960 R. Schiemann, D. Storkey, L. Thorpe, I. G. Watterson, D. N. Walters, A. West, R. A. Wood, T. Woollings, and P. K. Xavier. The
961 Met Office Global Coupled Model 3.0 and 3.1 (GC3.0 and GC3.1) Configurations. *Journal of Advances in Modeling Earth
962 Systems*, 10(2):357–380, 2018. doi: <https://doi.org/10.1002/2017MS001115>. URL <https://agupubs.onlinelibrary.wiley.com/doi/abs/10.1002/2017MS001115>.
- 964 G. Wolf, S. Ferrett, J. Methven, T. H. A. Frame, C. E. Holloway, O. Martinez-Alvarado, and S. J. Woolnough. Comparison
965 of probabilistic forecasts of extreme precipitation for a global and convection-permitting ensemble and hybrid statisti-
966 cal-dynamical method based on equatorial wave information. *Quarterly Journal of the Royal Meteorological Society*, n/a
967 (n/a), 2023. doi: <https://doi.org/10.1002/qj.4627>. URL <https://rmets.onlinelibrary.wiley.com/doi/abs/10.1002/qj.4627>.
- 969 G.-Y. Yang and Julia Slingo. The Diurnal Cycle in the Tropics. *Monthly Weather Review*, 129(4):784 – 801, 2001. doi: 10.
970 1175/1520-0493(2001)129<0784:TDCITT>2.0.CO;2. URL https://journals.ametsoc.org/view/journals/mwre/129/4/1520-0493_2001_129_0784_tdcitt_2.0.co_2.xml.
- 972 C. Zhang and J. Ling. Barrier Effect of the Indo-Pacific Maritime Continent on the MJO: Perspectives from Tracking MJO
973 Precipitation. *Journal of Climate*, 30(9):3439 – 3459, 2017. doi: 10.1175/JCLI-D-16-0614.1. URL <https://journals.ametsoc.org/view/journals/clim/30/9/jcli-d-16-0614.1.xml>.